A&A 652, A127 (2021)
https://doi.org/10.1051/0004-6361/202141145

Astronomy & Astrophysics

Populating the brown dwarf and stellar boundary: Five stars with transiting companions near the hydrogen-burning mass limit

Nolan Grieves[1], François Bouchy[1], Monika Lendl[1], Theron Carmichael[2,3], Ismael Mireles[4], Avi Shporer[5], Kim K. McLeod[6], Karen A. Collins[3], Rafael Brahm[7,8], Keivan G. Stassun[9], Sam Gill[10,11], Luke G. Bouma[12], Tristan Guillot[13], Marion Cointepas[1,14], Leonardo A. Dos Santos[1], Sarah L. Casewell[15], Jon M. Jenkins[16], Thomas Henning[17], Louise D. Nielsen[1], Angelica Psaridi[1], Stéphane Udry[1], Damien Ségransan[1], Jason D. Eastman[3], George Zhou[3], Lyu Abe[13], Abelkrim Agabi[13], Gaspar Bakos[12,18,19], David Charbonneau[3], Kevin I. Collins[18,19], Knicole D. Colon[20], Nicolas Crouzet[21], Georgina Dransfield[22], Phil Evans[23], Robert F. Goeke[5], Rhodes Hart[24], Jonathan M. Irwin[3], Eric L. N. Jensen[25], Andrés Jordán[7,8], John F. Kielkopf[26], David W. Latham[3], Wenceslas Marie-Sainte[27], Djamel Mékarnia[13], Peter Nelson[28], Samuel N. Quinn[3], Don J. Radford[29], David R. Rodriguez[30], Pamela Rowden[31], François–Xavier Schmider[13], Richard P. Schwarz[32], Jeffrey C. Smith[33,16], Chris Stockdale[34], Olga Suarez[13], Thiam-Guan Tan[35], Amaury H. M. J. Triaud[22], William Waalkes[36], and Geof Wingham[37]

(Affiliations can be found after the references)

Received 21 April 2021 / Accepted 5 July 2021

ABSTRACT

We report the discovery of five transiting companions near the hydrogen-burning mass limit in close orbits around main sequence stars originally identified by the Transiting Exoplanet Survey Satellite (TESS) as TESS objects of interest (TOIs): TOI-148, TOI-587, TOI-681, TOI-746, and TOI-1213. Using TESS and ground-based photometry as well as radial velocities from the CORALIE, CHIRON, TRES, and FEROS spectrographs, we found the companions have orbital periods between 4.8 and 27.2 days, masses between 77 and 98 $M_{\rm Jup}$, and radii between 0.81 and 1.66 $R_{\rm Jup}$. These targets have masses near the uncertain lower limit of hydrogen core fusion (~73-96 $M_{\rm Jup}$), which separates brown dwarfs and low-mass stars. We constrained young ages for TOI-587 (0.2 ± 0.1 Gyr) and TOI-681 (0.17 ± 0.03 Gyr) and found them to have relatively larger radii compared to other transiting companions of a similar mass. Conversely we estimated older ages for TOI-148 and TOI-746 and found them to have relatively smaller companion radii. With an effective temperature of 9800 ± 200 K, TOI-587 is the hottest known main-sequence star to host a transiting brown dwarf or very low-mass star. We found evidence of spin-orbit synchronization for TOI-148 and TOI-746 as well as tidal circularization for TOI-148. These companions add to the population of brown dwarfs and very low-mass stars with well measured parameters ideal to test formation models of these rare objects, the origin of the brown dwarf desert, and the distinction between brown dwarfs and hydrogen-burning main sequence stars.

Key words. brown dwarfs – stars: low-mass – binaries: eclipsing

1. Introduction

Brown dwarfs are objects with masses in between giant planets and low-mass stars. They are often defined with a lower limit of ~13 $M_{\rm Jup}$, the approximate mass at which an object can begin to ignite deuterium fusion in its core, and with an upper limit of ~80 $M_{\rm Jup}$, the approximate mass at which an object becomes sufficiently massive to fuse hydrogen nuclei into helium nuclei within its core: the principal characteristic of a main-sequence star. However, these boundaries are not clear-cut as the exact masses where deuterium and hydrogen fusion occur depend on the chemical composition of the object (e.g., Baraffe et al. 2002; Spiegel et al. 2011; Dieterich et al. 2014). A defining characteristic of brown dwarfs is their relative low occurrence rate ($\lessapprox$1%) in close orbits ($\lessapprox$5 AU) around main-sequence stars compared to giant planets and other stars, or the 'brown dwarf desert' (e.g., Marcy & Butler 2000; Grether & Lineweaver 2006; Sahlmann et al. 2011; Santerne et al. 2016; Grieves et al. 2017), with recent studies finding a dry desert for periods <100 days (e.g., Kiefer et al. 2019, 2021).

The relative lack of brown dwarf companions may be related to a transition of the formation mechanisms required to form giant planets and low-mass stars. In this case, lower mass brown dwarfs may form similar to giant planets via core accretion (Pollack et al. 1996) or disk instability (Cameron 1978; Boss 1997) and higher mass brown dwarfs may form similar to stars from gravitational collapse and turbulent fragmentation of molecular clouds (Padoan & Nordlund 2004; Hennebelle & Chabrier 2008). The boundary of these formation mechanisms is unclear and certainly depends on an object's initial environment.

Using a statistical study of 62 brown dwarfs Ma & Ge (2014) found the "driest" part of the desert in the mass range $35\ M_{\rm Jup} < M_{\rm b} \sin i < 55\ M_{\rm Jup}$ with periods less than 100 days. Ma & Ge (2014) also suggest 42.5 $M_{\rm Jup}$ may represent a transition between brown dwarfs that formed more similar to giant planets and those that formed more similar to main-sequence stars, as

they found that brown dwarfs with masses above 42.5 $M_{\rm Jup}$ have an eccentricity distribution more consistent with binaries. However, Ma & Ge (2014) were limited by a small sample size and more brown dwarfs have been found even in the driest part of the desert (e.g., Persson et al. 2019; Carmichael et al. 2019). Other studies have also suggested two separate populations for lower and higher mass brown dwarfs based on metallicity and eccentricity distributions (e.g., Maldonado & Villaver 2017; Kiefer et al. 2021). Conversely, some studies have suggested a more continuous formation between giant planets and low-mass stars where giant planets range from 0.3–60 or 73 $M_{\rm Jup}$ based on a continuum of their mass-density relation (Hatzes & Rauer 2015; Persson et al. 2019). While Whitworth (2018) argues brown dwarfs should not be distinguished from hydrogen-burning stars as they have more similarities to stars than planets.

Individual well-characterized brown dwarfs and very low-mass stars provide crucial insight into these possible formation scenarios. Particularly transiting brown dwarfs whose radii can be precisely determined allowing for a better interpretation of models. Whereas brown dwarfs detected only with radial velocities do not have clearly defined upper mass limits and may actually be low-mass stars (e.g., Kiefer et al. 2021). Space-based photometric missions are ideal to find these rare objects given their robust photometric precision and long uninterrupted observations, and recent missions such as *Kepler* (Borucki et al. 2010) and K2 (Howell et al. 2014) have led to successful follow-up mass measurements of transiting brown dwarfs (e.g., Bayliss et al. 2017; Cañas et al. 2018; Carmichael et al. 2019; Persson et al. 2019). The currently operating space-based all-sky Transiting Exoplanet Survey Satellite (TESS; Ricker et al. 2015) has continued to populate the sparse desert with well-characterized brown dwarfs and very low-mass stars (e.g., Šubjak et al. 2020; Carmichael et al. 2020, 2021; Mireles et al. 2020).

We report the discovery of five transiting companions with masses close to the upper boundary of the brown dwarf regime that were each first identified as TESS objects of interest (TOIs): TOI-148, TOI-587, TOI-681, TOI-746, and TOI-1213. Each object has robust photometric and spectroscopic measurements allowing precisely determined characteristics, and given their close proximity to the hydrogen-burning limit they are ideal to test current formation models and comparisons between brown dwarfs and low-mass stars. In Sect. 2 we describe our photometry, spectroscopy, and imaging observations. In Sect. 3 we detail our analysis of the systems including the host stars and their companions. In Sect. 4 we discuss our results and in Sect. 5 we give our conclusions.

2. Observations

2.1. TESS photometry

In this section we describe the TESS observations for each star. We refer the reader to Tables A.2–A.6 for the stellar parameters and properties of each star. We display phased TESS photometry for all five of our stars with transiting companions as well as transit observations from all available ground-based photometry, described in Sect. 2.2, in Figs. 1–5. We obtained TESS photometry from exomast[1], which is part of the Barbara A. Mikulski Archive for Space Telescopes (MAST) astronomical data archive hosted by the Space Telescope Science Institute.

TOI-148 (TIC 393 940 766) was observed by TESS in Sector 1 (UT 2018 July 25 to UT 2018 August 22) and the light curve

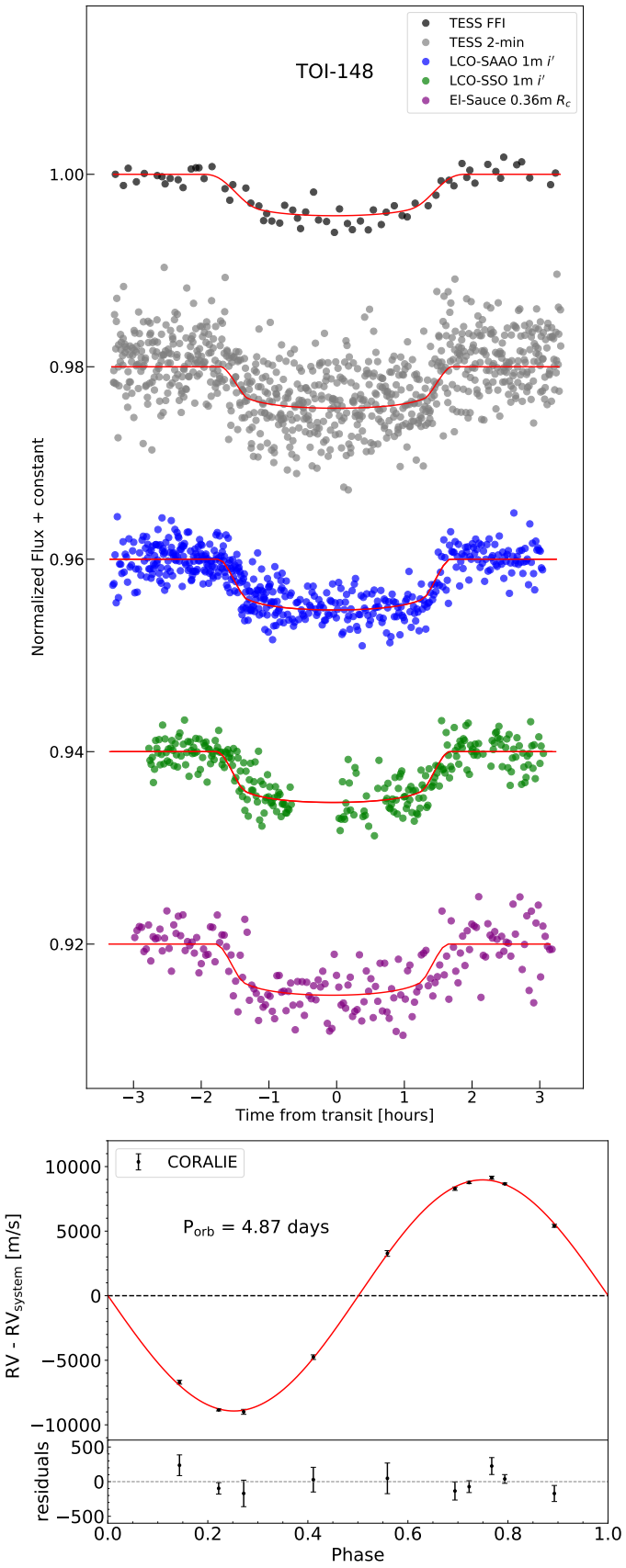

Fig. 1. TOI-148 light curves (*top*) and RVs (*bottom*) phased to the companion's orbital period. The red lines in the upper plot show the best-fit transit model to each photometry data set from our EXOFASTv2 analysis described in Sect. 3.4.1. In the lower plot the red line shows the best-fit Keplerian model to the RVs from our EXOFASTv2 analysis.

[1] https://exo.mast.stsci.edu

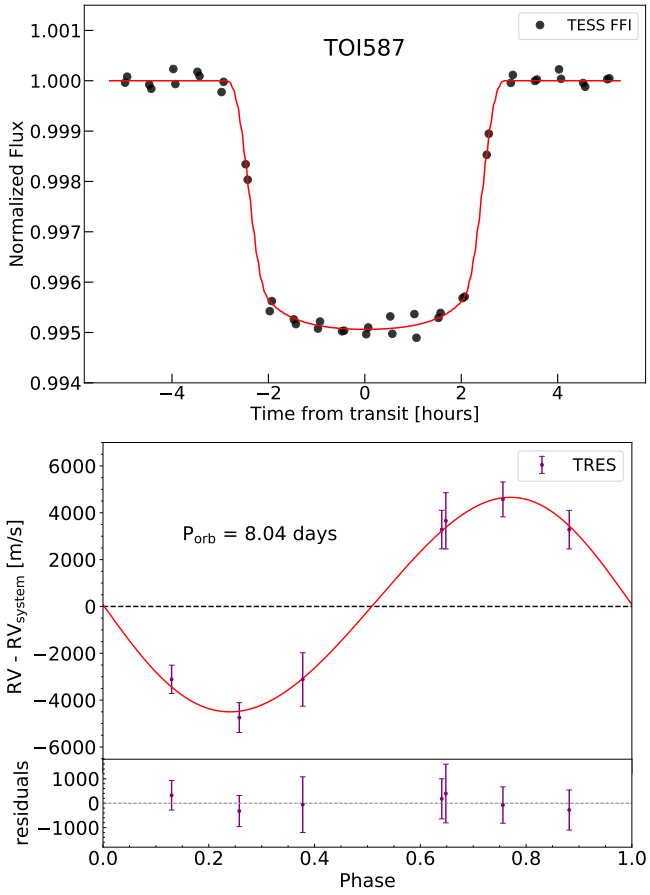

Fig. 2. TOI-587 light curves (*top*) and RVs (*bottom*) phased to the companion's orbital period. The red lines display our best-fit models from EXOFASTv2 as described in Fig. 1.

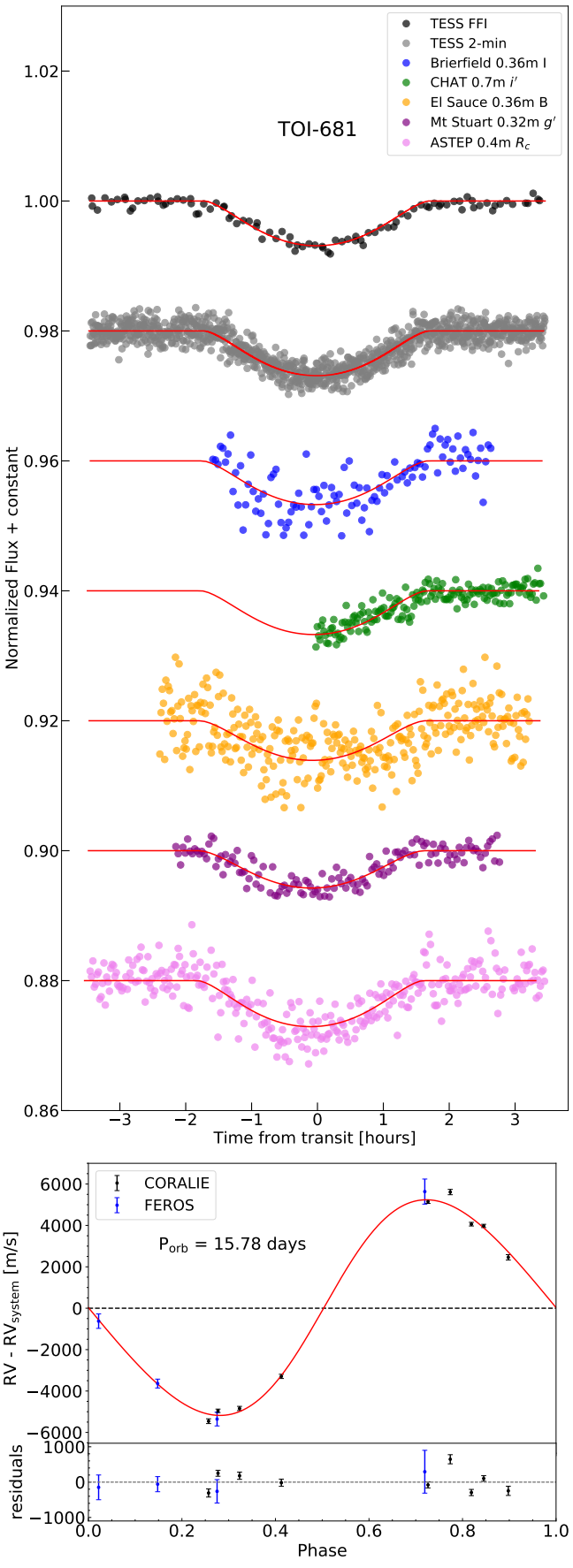

Fig. 3. TOI-681 light curves (*top*) and RVs (*bottom*) phased to the companion's orbital period. The red lines display our best-fit models from EXOFASTv2 as described in Fig. 1.

was derived from Full Frame Image (FFI) observations with a cadence of 30 min and processed by the Quick Look Pipeline (QLP; Huang et al. 2020a,b). QLP transits were identified with a high signal to noise ratio every 4.87 days for a total of six transits detected in the QLP data. TOI-148 was observed again by TESS in Sector 28 (UT 2020 July 31 to UT 2020 August 25) with 2-min cadence exposures. The 2-min data were processed by the Science Processing Operations Center (SPOC; Jenkins et al. 2016) pipeline which produces two light curves per sector called Simple Aperture Photometry (SAP) and Presearch Data Conditioning Simple Aperture Photometry (PDCSAP; Smith et al. 2012; Stumpe et al. 2012, 2014). We use the PDCSAP light curves for our analysis. The SPOC pipeline detected the transit signatures in the transit search pipeline (Jenkins 2002; Jenkins et al. 2010) and these transit signatures were fit to a limb-darkened transit model (Li et al. 2019). The transit fits passed all of the data validation module's diagnostic tests (Twicken et al. 2018), including the difference image centroiding test, which localized the source of the transit signal to within 1.23 ± 2.6 arcsec. This difference image centroiding test complements the speckle interferometry results in Sect. 2.4. A total of four transits were detected in the 2-min cadence data; we note a ~5 day gap in the middle of the TESS Sector 28 data. No secondary transit or eclipse was detected above 3.3σ (426 ppm), and no additional transit signals were detected in the multiplanet transit search.

TOI-587 (TIC 294 090 620) was observed in TESS Sector 8 (UT 2019 February 2 to UT 2019 February 28) with FFI

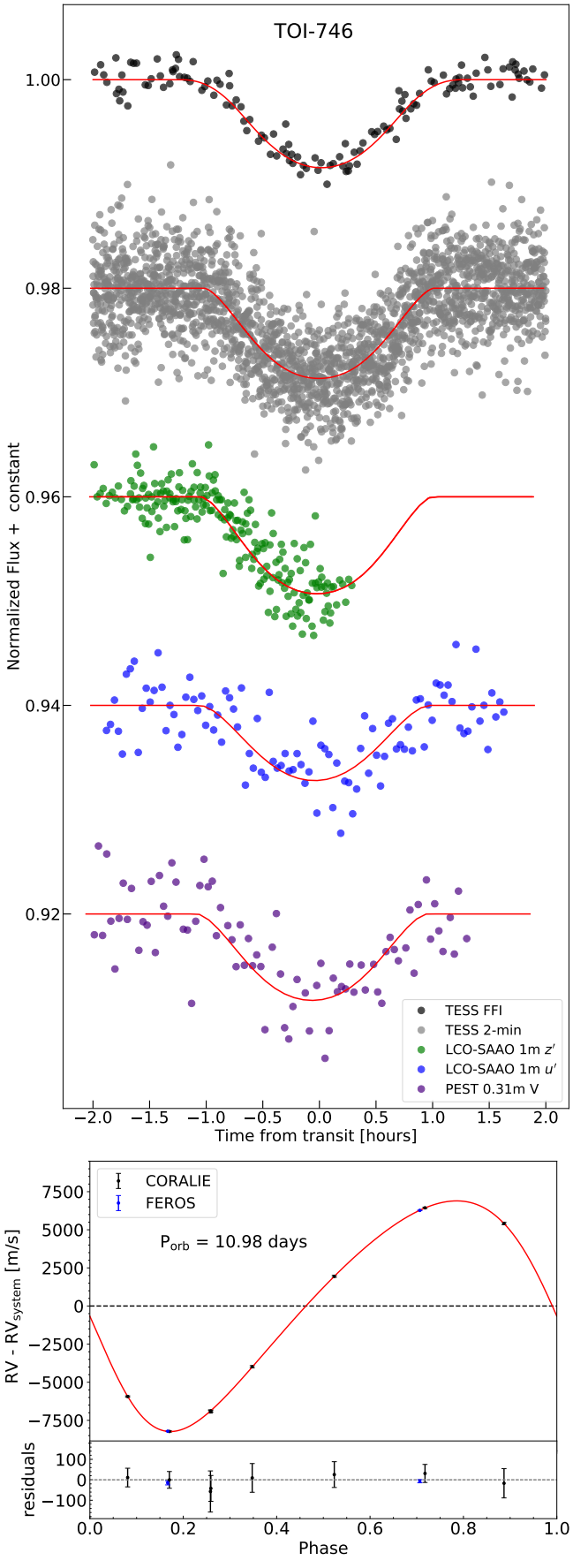

Fig. 4. TOI-746 light curves (*top*) and RVs (*bottom*) phased to the companion's orbital period. The red lines display our best-fit models from EXOFASTv2 as described in Fig. 1.

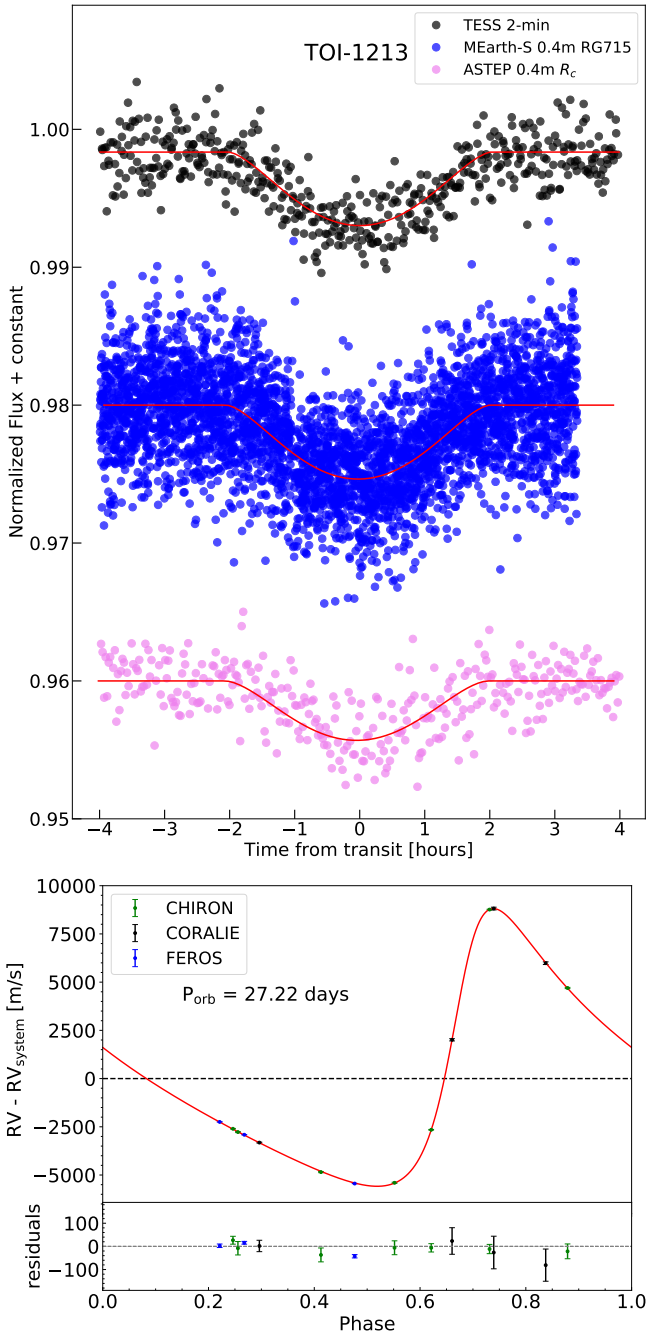

Fig. 5. TOI-1213 light curves (*top*) and RVs (*bottom*) phased to the companion's orbital period. The red lines display our best-fit models from EXOFASTv2 as described in Fig. 1.

observations. Two transits with a depth of ~0.5% were identified in the QLP processed light curve with a separation 8.0 days.

TOI-681 (TIC 410 450 228) was observed in TESS Sectors 8 (UT 2019 February 2–7), 9 (UT 2019 February 28 to UT 2019 March 26), 27 (UT 2020 July 5–30), and 31 (UT 2020 October 22 to UT 2020 November 18) with 2-min cadence exposures. The 2-min data were processed by SPOC which identified two 1% deep transits 15.8 days apart. TOI-681 was also observed with FFI observations in Sectors 1 (UT 2018 July 25 to UT 2018 August 22), 4 (UT 2018 October 19 to UT 2018 November 15), 5 (UT 2018 November 15 to UT 2018 December 11), 7 (UT 2019 January 7 to UT 2019 February 1), 10 (UT 2019 March 26 to UT 2019 April 21), and 11 (UT 2019 April 22 to UT 2019 May

Table 1. Summary of ground-based photometric follow-up observations.

Telescope	Location	Date [UTC]	Filter	Aperture radius [arcsec]	Coverage
TOI 148.01 (TIC 393 940 766)					
LCO-SAAO 1 m	South Africa	2020-06-07	i'	4.7	Ingress
LCO-SSO 1 m	Australia	2020-06-27	i'	5.1	Ingress
LCO-SSO 1 m	Australia	2020-07-02	i'	4.7	Egress
El-Sauce 0.36 m	Chile	2020-07-12	R_c	5.9	Full
LCO-SAAO 1 m	South Africa	2020-07-21	i'	4.3	Full
TOI 681.01 (TIC 410 450 228)					
Brierfield 0.36 m	Australia	2019-10-26	I	10.3	Ffull
CHAT 0.7 m	Chile	2019-11-26	i'	8.4	Egress
El Sauce 0.36 m	Chile	2019-11-27	B	7.4	Full
Mt. Stuart 0.32 m	New Zealand	2020-04-01	g'	4.4	Full
ASTEP 0.4 m	Antarctica	2020-06-19	R_c	10.2	Full
TOI 746.01 (TIC 167 418 903)					
LCO-SAAO 1 m	South Africa	2019-02-18	z'	6.2	Ingress
LCO-SAAO 1 m	South Africa	2019-03-01	u'	5.9	Full
LCO-SAAO 1 m	South Africa	2019-04-25	z'	5.9	ingress
PEST 0.31 m	Australia	2020-10-25	V	7.4	Full
TOI 1213.01 (TIC 399 144 800)					
MEarth-S 0.4 m	Chile	2020-02-23	RG715	5.0	Full
ASTEP 0.4 m	Antarctica	2020-08-04	R_c	10.2	Full

Notes. Observatory acronyms: ASTEP–Antarctic Search for Transiting ExoPlanets; CHAT–Chilean-Hungarian Automated Telescope; LCO–Las Cumbres Observatory; PEST–Perth Exoplanet Survey Telescope.

20). The transit signature passed all the data validation diagnostic tests and was localized to within 0.726 ± 2.5 arcsec in the multisector 8 and 9 search. No statistically weak secondary was detected above the 3.3 sigma (426 ppm) level, and no further transiting planet signatures were detected in the multiplanet search. This star was also observed in sector 27 but only one transit was observed. It was re-observed in sector 31, passed all the data validation diagnostic tests, including the difference image centroiding that localized the source to within 0.958 ± 2.5 arcsec, and no statistically significant weak secondaries were detected above the 2.8σ (629 ppm) level.

TOI-746 (TIC 167 418 903) was observed by TESS in Sectors 1–13 (UT 2018 July 25 to UT 2019 July 17) with FFI observations as well as 2-min cadence exposures in Sectors 11–13 (UT 2019 May 21 to UT 2019 July 17) and 28–33 (UT 2020 July 31 to UT 2021 January 13). The FFI observations of all sectors were processed by the QLP and the 2-min data were processed with the SPOC pipeline, both showing a transit-like event occurring every 10.98 days. We detected 17 transits in the FFI data and 11 transits in the 2-min data.

TOI-1213 (TIC 399 144 800) was observed by TESS in Sectors 10 and 11 (UT 2019 March 26 to UT 2019 May 21) with 2-min cadence exposures. The 2-min data was processed by the SPOC pipeline, which showed one transit-like event in each sector, spaced 27.214 days apart. The multisector data validation report for sectors 10 and 11 indicated that the transit signature passed all the DV diagnostic tests, localized the source to within 3.8 ± 2.1 arcsec, and detected no weak secondaries above 3.1σ (435 ppm), and no additional transiting planet signatures were found.

2.2. Ground-based photometric follow-up

We acquired ground-based time-series photometry of TOI-148, TOI-681, TOI-746, and TOI-1213 as part of the *TESS* Follow-up Observing Program (TFOP)[2]. The TFOP's Sub Group 1 (SG1; seeing-limited photometry) group includes observers at more than a hundred telescopes distributed around the world. TFOP SG1 partners choose targets to follow up using the `TESS Transit Finder`, which is a customized version of the `Tapir` software package (Jensen 2013). Photometric data are extracted by each observer most often using the `AstroImageJ` (`AIJ`) software package (Collins et al. 2017). Data and analysis notes are uploaded to the ExoFOP-TESS[3] repository and submitted to the SG1 team for validation.

In the case of the objects described here, we used the observations to rule out nearby eclipsing binaries as sources of the TESS signal, confirm the events on target, determine the *TESS* photometric deblending factors for each field, place constraints on transit depth differences across optical filter bands, and refine the *TESS* ephemerides by extending the time baselines. We summarize the observations that resulted in data useful for fitting in Table 1 and we plot the resulting light curves in Figs. 1 and 3–5.

The optimal photometric aperture radii used to extract light curves for these targets depends on the combination of pixel size, seeing disk size, focus (some observations are intentionally defocused to avoid saturation in the case of very bright targets), and the presence of on-sky neighbors visible in the images. We

[2] https://tess.mit.edu/followup
[3] https://exofop.ipac.caltech.edu/tess/

checked the apertures listed in Table 1 against the *Gaia* DR2 catalog to determine the extent to which they might be contaminated by other stars. In the case of TOI-681, there is a *Gaia* neighbor 7″ away, and so inside most of the apertures used; however, at 6.4 magnitudes fainter than the target, the contribution is negligible within the photometric precision. Similarly, in the case of TOI-746, there is a possible *Gaia* blend at a separation of 6 arcsec, just at the edge of the apertures used, but at 8.8 magnitudes fainter it is insignificant. We describe checks for smaller-separation neighbors in Sect. 2.4.

2.3. Spectroscopic follow-up and radial velocities

We obtained spectra and radial velocities of the five stars using observations from the 1.5 m SMARTS/CHIRON, Euler 1.2 m/CORALIE, MPG/ESO 2.2 m/FEROS, and 1.5 m SAO Tillinghast/TRES facilities. We summarize the radial velocity (RV) measurements of each star in Table A.1 and each star's phased radial velocities with their best Keplerian fits (see Sect. 3) are displayed in Figs. 1–5.

For TOI-148, TOI-681, TOI-746, and TOI-1213, we obtained RVs with the high resolution CORALIE spectrograph on the Swiss 1.2 m Euler telescope at La Silla Observatory, Chile (Queloz et al. 2001). CORALIE has a resolution of $R \sim 60\,000$ and is fed by two fibers: a 2 arcsec on-sky science fiber encompassing the star and another fiber that can either connect to a Fabry-Pérot etalon for simultaneous wavelength calibration or on-sky for background subtraction of sky flux. We observed all four stars in the simultaneous Fabry-Pérot wavelength calibration mode. The spectra were reduced with the CORALIE standard reduction pipeline and RVs were computed for each epoch by cross-correlating with a binary G2 mask (Pepe et al. 2002).

We obtained 11 CORALIE observations for TOI-148 from UT 2018 September 23 to UT 2019 July 15. Nine CORALIE observations of TOI-681 were obtained from UT 2019 May 19 to UT 2020 March 15. We obtained eight CORALIE observations for TOI-746 from UT 2019 October 21 to UT 2020 March 12. TOI-1213 was observed four times with CORALIE from UT 2020 February 4 to UT 2020 March 17.

We used the TRES instrument on Mt. Hopkins, Arizona to obtain reconnaissance spectra for TOI-587. TRES has a resolving power of $R \sim 44\,000$ and covers a wavelength range of 390–910 nm. We use multiple echelle orders for each spectrum to measure a relative RV at each phase in the orbit of the transiting companion. We visually review each individual order to omit those with low signal-to-noise per resolution element (S/N) and we remove obvious cosmic rays. Each order is cross-correlated with the highest S/N spectrum of the star and then the average RV of all the orders per spectrum is taken as the RV of the star at a given orbital phase. The spectra of TOI-587 were taken between UT 2019 April 16 and UT 2019 April 30 with exposure times of 150 s and 360 s, giving a signal-to-noise per resolution element between 66 and 117.

TOI-618, TOI-746, and TOI-1213 were monitored with the FEROS spectrograph (Kaufer et al. 1999) mounted on the MPG 2.2 m telescope in the ESO La Silla Observatory. These observations were performed between June of 2019 and March of 2020 in the context of the Warm gIaNts with tEss (WINE) collaboration which focuses in the discovery and orbital characterization of transiting planets with period longer than ≈10 days (e.g., Jordán et al. 2020; Brahm et al. 2020; Schlecker et al. 2020).

We obtained between two and four spectra per target on different epochs in order to determine if they presented radial velocity variations consistent to those produced by an orbiting planetary companion. All observations were executed with the simultaneous calibration technique, where a second fiber is illuminated with a Thorium-Argon lamp to trace instrumental velocity drifts during the exposure. The exposure times adopted were 400 s, 1200 s, and 900s , for TOI-618, TOI-746, and TOI-1213, respectively. The FEROS data were processed from raw images to precision radial velocities with the `ceres` pipeline (Brahm et al. 2017). We used a G2-type binary mask as a template to compute the radial velocities through the cross-correlation technique. We also obtained line bisector span measurements from the cross-correlation function. These observations showed that these three systems were presenting radial velocity variations with amplitudes larger than those produced by planet mass companions, and therefore were dropped from the queue of the WINE project.

TOI-1213 was observed with the CTIO High Resolution spectrometer (CHIRON; Tokovinin et al. 2013; Paredes 2021), mounted on the CTIO 1.5-meter Small and Moderate Aperture Research Telescope System (SMARTS) telescope. CHIRON is a fiber-fed high resolution echelle spectrograph, with a resolving power of $R = 8000$ and a wavelength range of 410 nm to 870 nm. The target was observed by CHIRON 7 times, three times between UT 2020 February 7 and UT 2020 March 9, and four times between UT 2020 December 8 and UT 2020 December 25. Each observation was composed of 3 × 20 min exposures. The spectral extraction was performed by the default CHIRON pipeline (Piskunov & Valenti 2002), and the RVs were derived from the CHIRON spectra by a least-squares deconvolution technique (Zhou et al. 2020), and are listed in Table A.1.

2.4. High-resolution imaging

We used speckle imaging from the high resolution camera (HRCam; Tokovinin 2018) mounted on the southern astrophysical research (SOAR) 4.1 m telescope in Cerro Pachón, Chile to verify there are no stars close to our targets that would significantly contaminate the transit or RV signals we observe. The relatively large 21″ pixels of TESS can result in photometric contamination causing astrophysical false positives such as a background or nearby eclipsing binary stars if they fall within the same TESS image profile as the target. Close contaminants can also lead to inaccurate estimates of the transit depth from a diluted transit in a blended light curve.

All five targets were observed with HRCam, which uses the speckle interferometry techniques in a visible bandpass similar to that of TESS. Ziegler et al. (2020) provides a description of HRCam observations of TESS targets with data reduction described in Tokovinin (2018). SOAR speckle imaging was obtained on UT 2018 September 24 for TOI-148, UT 2019 May 18 for both TOI-587 and TOI-681, UT 2020 January 7 for TOI-746, and UT 2019 December 12 for TOI-1213. We detect no nearby starts within 3″ for all five stars. We show the 5σ detection sensitivity and the speckle auto-correlation function from the SOAR observations in Fig. 6.

3. Analysis

3.1. Spectral analysis

We derived stellar parameters including effective temperature $T_{\rm eff}$, surface gravity $\log g_*$, and metalicity [Fe/H] using

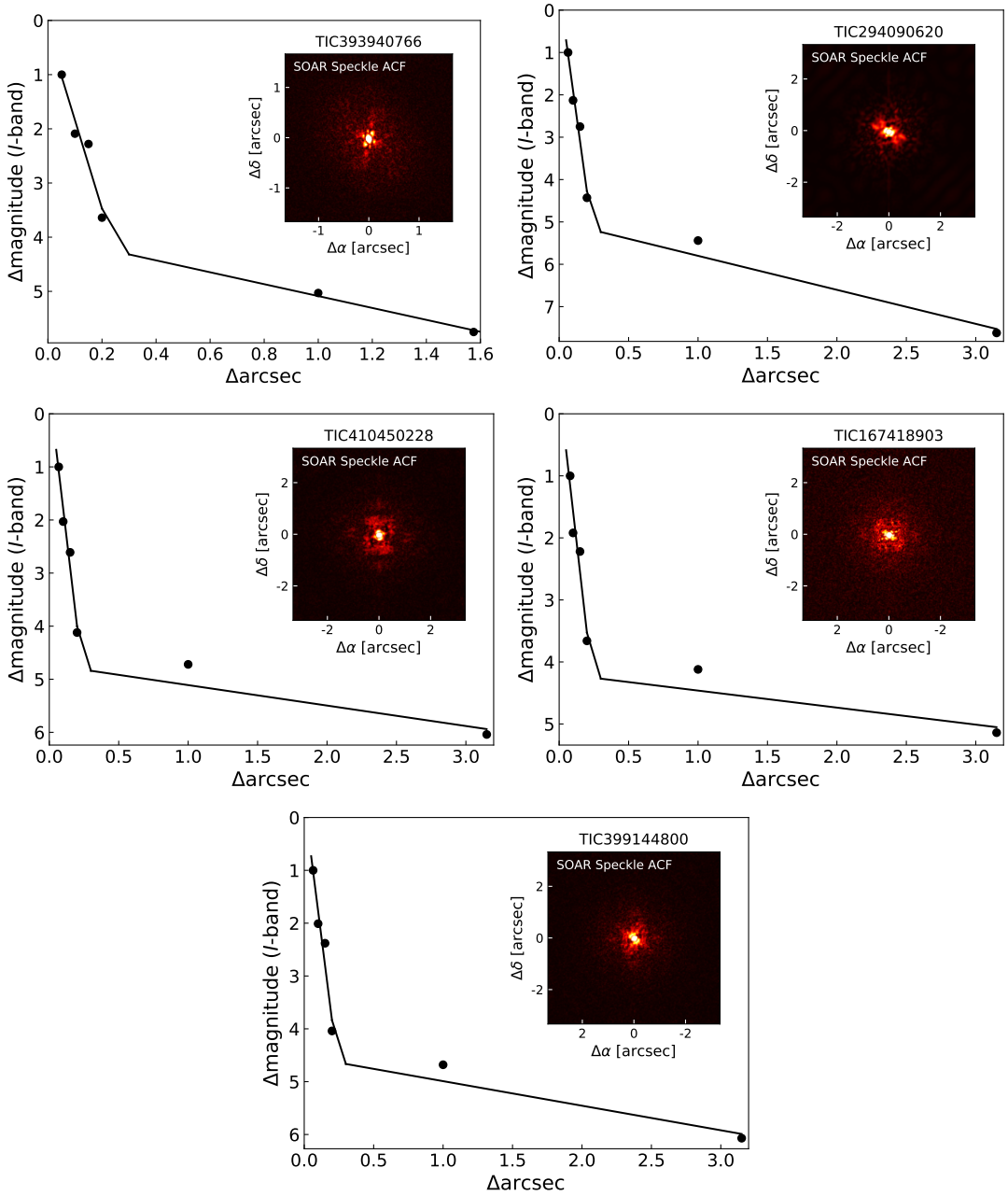

Fig. 6. SOAR/HRCam speckle interferometry imaging with *I*-band autocorrelation functions (Ziegler et al. 2020) for TOI-148 (TIC 393 940 766; *top left*), TOI-587 (TIC 294 090 620; *top right*), TOI-681 (TIC 410 450 228; *middle left*), TOI 746 (TIC 167 418 903; *middle right*), and TOI 1213 (TIC 399 144 800; *bottom*). The 5σ contrast curves with a linear fit are shown with black solid lines. The auto-correlation functions obtained in *I*-band are shown within the contrast curve plots.

SpecMatch-Emp (Yee et al. 2017) on CORALIE spectra for TOI-148, TOI-746, and TOI-1213. Spectra were coadded onto a common wavelength axis to increase signal-to-noise prior to spectral analysis. SpecMatch-Emp uses a large library of stars with well-determined parameters to match the input spectra and derive spectral parameters. We use a spectral region that includes the Mg I b triplet (5100–5400 Å) to match our spectra. SpecMatch-Emp uses χ^2 minimisation and a weighted linear combination of the five best matching spectra in the SpecMatch-Emp library to determine $T_{\rm eff}$, $\log g_*$, and [Fe/H].

We also determine $T_{\rm eff}$, $\log g_*$, and [Fe/H] using coadded CORALIE spectra for TOI-148, TOI-746, and TOI-1213 with the analysis package iSpec (Blanco-Cuaresma et al. 2014). We used the synthesis method to fit individual spectral lines of the coadded spectra. For TOI-148, TOI-746, and TOI-1213 we used the radiative transfer code SPECTRUM (Gray & Corbally 1994) to generate model spectra with MARCS model atmospheres (Gustafsson et al. 2008), version 5 of the GES (*Gaia* ESO survey) atomic line list provided within iSpec and solar abundances from Asplund et al. (2009). Using the same method as Grieves et al. (2021), we combine the iSpec analysis results and SpecMatch-Emp results for TOI-148, TOI-746, and TOI-1213. In order to create wide uncertainties we include the entire uncertainty range of both results that includes the lowest and highest uncertainty values of both methods. We present these spectroscopically derived parameters in Table 2.

Table 2. Stellar parameters derived from spectra.

Star	$T_{\rm eff}$ [K]	[Fe/H] dex	$\log g_*$ [cgs]	$v \sin i_*$ [km^{-1}]	Source
TOI-148	5836 ± 286	−0.28 ± 0.28	4.11 ± 0.37	10.1 ± 0.8	CORALIE
TOI-587	10 400 ± 300	0.07 ± 0.12	4.20 ± 0.30	34.0 ± 2.0	TRES
TOI-681	7297 ± 45	−0.12 ± 0.05	4.32 ± 0.14	30.8 ± 0.8	GALAH DR2
TOI-746	5593 ± 215	0.01 ± 0.29	4.30 ± 0.29	6.1 ± 1.2	CORALIE
TOI-1213	5430 ± 215	0.28 ± 0.16	4.47 ± 0.26	4.0 ± 1.2	CORALIE

Notes. We refer the reader to the final adopted parameters for each star presented in Tables A.2–A.6. TOI-148, TOI-746, and TOI-1213 parameters were obtained from CORALIE spectra by combining the analysis results of both SpecMatch-Emp (Yee et al. 2017) and with an iSpec (Blanco-Cuaresma et al. 2014) analysis. The high temperature of TOI-587 precluded using SpecMatch-Emp and iSpec analysis and we use a separate analysis described in Sect. 3.1 on the TRES spectra. For TOI-681 we use GALAH DR2 results (Buder et al. 2018).

TOI-587 is a very hot star which is outside the range of temperatures in the spectral library of SpecMatch-Emp. TOI-587 also falls outside the valid temperature range for the MARCS model atmospheres and we instead use the ATLAS9 model atmospheres Castelli & Kurucz (2004). Macroturbulence was estimated using Eq. (5.10) from Doyle et al. (2014) and microturbulence was accounted for at the synthesis stage using Eq. (3.1) from the same source. The Hα, NaID and Mg I b lines were used to infer the effective temperature $T_{\rm eff}$ and gravity $\log g_*$ while FeI and FeII lines were used to determine the metallicity [Fe/H] and the projected rotational velocity $v \sin i_*$. Trial synthetic model spectra were fit until an acceptable match to the data was found. Uncertainties were estimated by varying individual parameters until the model spectrum was no longer well-matched to the data.

For TOI-681 we use stellar parameters from GALAH DR2 (Buder et al. 2018) spectroscopy as we find these parameters more robust given their higher signal-to-noise ratio (S/N) compared to our CORALIE spectra. We do not find GALAH DR2 data for the other stars. Our wavelet analysis (Gill et al. 2018, 2019) is also able to determine surface rotational velocity $v \sin i_*$ from spectra which we apply to TOI-148, TOI-587, TOI-746, and TOI-1213 and present in Table 2. For TOI-681 we present the $v \sin i_*$ from GALAH DR2. We also examined the spectra and their cross-correlation functions (CCFs) with a binary template (e.g., Pepe et al. 2002) when available and do not find any evidence that the targets are double-lined spectroscopic binaries.

3.2. Spectral energy distribution analysis

As an independent check on the derived stellar parameters, we performed an analysis of the broadband spectral energy distributions (SEDs) of each star, together with the *Gaia* DR2 parallax in order to constrain the basic stellar parameters and to determine an empirical measurement of the stellar radius, following the procedures described in Stassun & Torres (2016); Stassun et al. (2017, 2018). We pulled the GALEX NUV and FUV fluxes, the $B_T V_T$ magnitudes from *Tycho*-2, the *BVgri* magnitudes from APASS, the JHK_S magnitudes from 2MASS, the W1–W4 magnitudes from WISE, and the $GG_{\rm BP}G_{\rm RP}$ magnitudes from *Gaia*. For the hottest source we also pulled the TD1/wide UV fluxes from the TD1 satellite (Thompson et al. 1978). Together, the available photometry spans the full stellar SED over the wavelength range 0.15–22 µm (see Fig. 7). We performed a fit using Kurucz stellar atmosphere models, with the priors on effective temperature ($T_{\rm eff}$), surface gravity ($\log g$), and metallicity ([Fe/H]) from the spectroscopic analysis. The remaining parameter is the extinction ($A_{\rm V}$), which we limited to the maximum line-of-sight extinction from the Galactic dust maps of Schlegel et al. (1998).

The resulting fits (Fig. 7) have small reduced χ^2 values reported in Table 3, which also summarizes the other resulting stellar parameters: Integrating the (unreddened) model SED gives the bolometric flux at Earth, $F_{\rm bol}$; taking the $F_{\rm bol}$ and $T_{\rm eff}$ together with the *Gaia* DR2 parallax, adjusted by +0.08 mas to account for the systematic offset reported by Stassun & Torres (2018), gives the stellar radius, $R_\star$. We can then infer the stellar mass, $M_\star$, empirically from $R_\star$ and $\log g$, as well as estimate it via the empirical relations of Torres et al. (2010).

We can also estimate the stellar rotation periods from the spectroscopic $v \sin i$ together with the above $R_\star$, giving an upper limit of $P_{\rm rot}/\sin i$. From the excess GALEX UV emission, when present, we can also estimate the chromospheric activity indicator, $R'_{\rm HK}$ via the empirical relations of Findeisen et al. (2011). In turn, these provide another estimate of the stellar rotation period via the empirical rotation-activity relations of Mamajek & Hillenbrand (2008). Finally, these activity measures provide an estimate of the stellar age, $\tau_\star$ again via the empirical activity-age relations of Mamajek & Hillenbrand (2008). However, we note the ages derived from stellar rotation and activity are likely underestimated due to the stellar rotations likely being affected by the companions (e.g., tidal locking) as discussed in Sect. 4.1.

3.3. TOI-681 kinematic analysis and cluster membership

TOI-681 has been previously reported to be a member of the open star cluster NGC 2516 (Gaia Collaboration 2018; Cantat-Gaudin et al. 2018; Kounkel & Covey 2019; Meingast et al. 2021). We reassessed its position and kinematics relative to NGC 2516 as follows. First, we collected the NGC 2516 members reported by Cantat-Gaudin et al. (2018). To define a set of reference "neighborhood" stars, we then queried *Gaia* DR2 for stars within 4 standard deviations of the mean values of NGC 2516's right ascension, declination, and parallax. The corresponding positions, proper motions, and *Gaia* DR2 radial velocities are shown in Fig. A.1.

TOI-681 is well within the cloud of cluster members (dark black points in Fig. A.1) in each dimension, rather than being within the outlying neighborhood (gray points). While TOI 681 did not have a *Gaia* DR2 RV, we measured a barycenter-corrected velocity with CORALIE of $22.120^{+0.096}_{-0.087}$ km s^{-1} and with FEROS of 23.75 ± 0.14 km s^{-1}. This is an independent line of support for the cluster membership, as the mean (*Gaia*-derived) cluster RV is 24.1 km s^{-1}. Independent age indicators for TOI-681 such as the photospheric lithium abundance or the

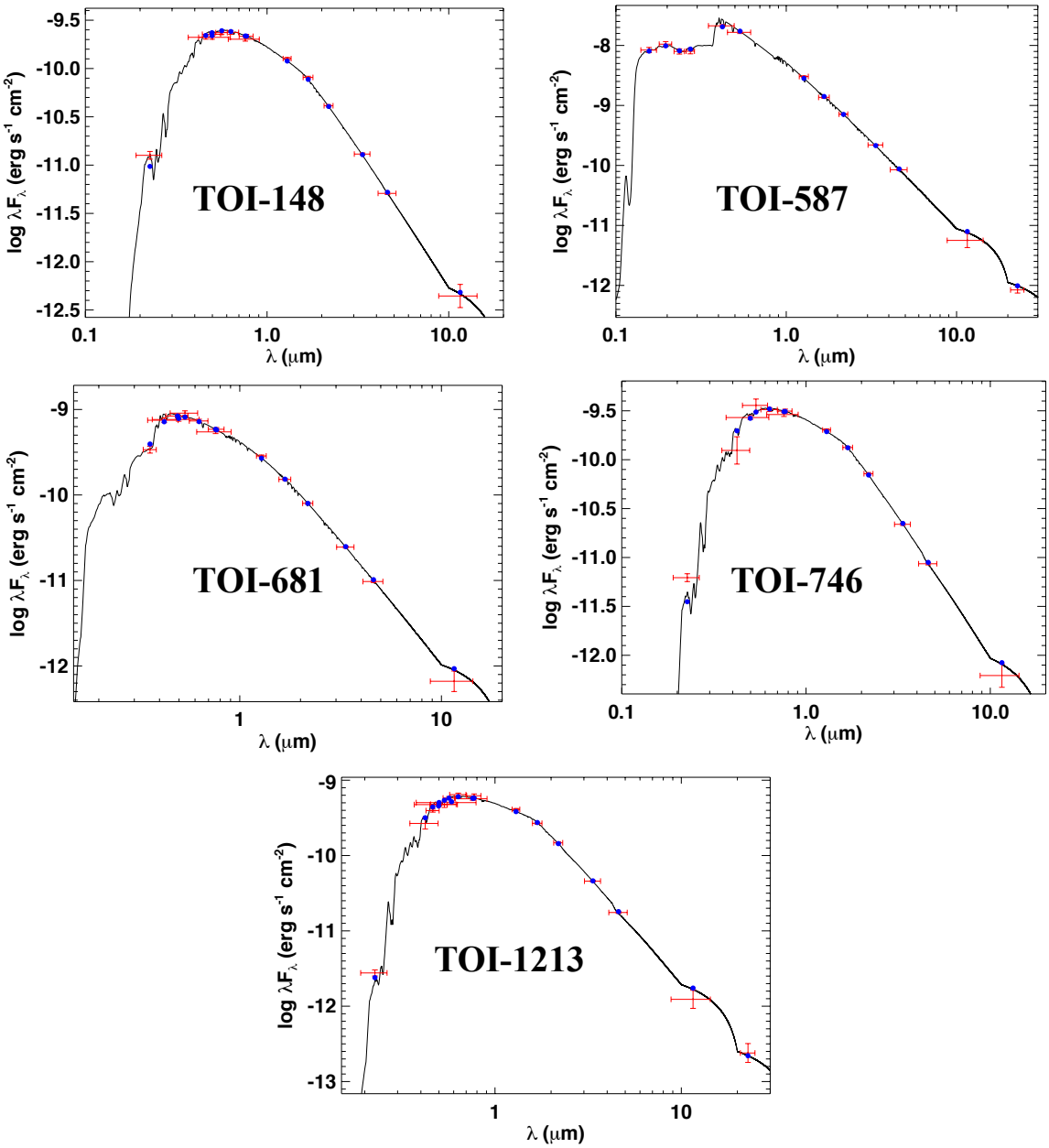

Fig. 7. Spectral energy distributions for TOI-148 (*top left*), TOI-587 (*top right*), TOI-681 (*middle left*), TOI-746 (*middle right*), and TOI-1213 (*bottom*). Red symbols represent the observed photometric measurements, where the horizontal bars represent the effective width of the bandpass. Blue symbols are the model fluxes from the best-fit Kurucz atmosphere model (black).

rotation period are not applicable due to the stellar type ($T_{\rm eff}$ ≈ 7400 K). Nonetheless, given the six-dimensional position and kinematic overlap with the other cluster members, we proceed under the assumption that TOI-681 is a member of NGC 2516.

Reported ages of NGC 2516 vary between 100 Myr and 300 Myr (Jeffries et al. 1997, 1998; Randich et al. 2018; Gaia Collaboration 2018; Kounkel & Covey 2019). While determining absolute ages for clusters is a challenging problem (Soderblom et al. 2014), NGC 2516 appears to be slightly older than the Pleiades based on the main sequence turn-off and gyrochronology (Cummings & Kalirai 2018; Fritzewski et al. 2020; Bouma et al., in prep.). The current consensus Pleiades age based on the main sequence turn-off and the lithium depletion boundary is 125 ± 20 Myr (see Soderblom et al. 2014). We therefore expect the age of NGC 2516 to be within the interval of 140–200 Myr. We adopt 170 ± 25 Myr and use this value as the age of TOI-681. This is older than the absolute model-averaged age of ≈90 Myr determined by Randich et al. (2018) using isochrones, which we suspect might be explained by the presence of blue-stragglers on the main sequence turn-off (Cummings & Kalirai 2018).

3.4. Global modeling

3.4.1. Modeling with EXOFASTv2

We derive companion parameters and final stellar parameters using EXOFASTv2 (Eastman et al. 2013, 2019; Eastman 2017). A full description of EXOFASTv2 is given in Eastman et al. (2019), which can fit any number of transit and RV sources while exploring the vast parameter space through a differential evolution Markov chain coupled with a Metropolis-Hastings Monte Carlo sampler. A built-in Gelman-Rubin statistic (Gelman &

Table 3. Stellar parameters derived from SED fitting and empirical relations.

Star	χ^2_ν	$T_{\rm eff}$ [K]	[Fe/H] dex	$\log g_*$ [cgs]	$A_{\rm V}$ mag	$F_{\rm bol}$ 10^{-10} [erg s^{-1} cm^{-2}]	$R_\star$ $R_\odot$
TOI-148	1.4	5975 ± 150	–0.50 ± 0.25	4.25 ± 0.1	0.03 ± 0.03	3.405 ± 0.079	1.192 ± 0.068
TOI-587	0.9	9800 ± 200	–0.10 ± 0.15	4.15 ± 0.15	0.02 ± 0.02	252.9 ± 5.9	2.031 ± 0.092
TOI-681	1.0	7390 ± 150	–0.25 ± 0.25	4.20 ± 0.15	0.22 ± 0.02	12.41 ± 0.14	1.586 ± 0.067
TOI-746	1.6	5700 ± 150	–0.25 ± 0.25	4.40 ± 0.10	0.18 ± 0.02	5.126 ± 0.059	0.957 ± 0.051
TOI-1213	1.2	5675 ± 175	0.00 ± 0.25	4.45 ± 0.10	0.34 ± 0.03	10.47 ± 0.12	0.951 ± 0.059

Star	$M_\star^{(a)}$ $M_\odot$	$M_\star^{(b)}$ $M_\odot$	$P_{\rm rot}/\sin i$ [d]	$\tau_\star^{(c)}$ [Gyr]	$R'_{\rm HK}$ dex	$\tau_\star^{(d)}$ [Gyr]
TOI-148	0.94 ± 0.26	1.03 ± 0.06	5.97 ± 0.47	0.55 ± 0.07	–	–
TOI-587	2.12 ± 0.29	2.32 ± 0.14	3.02 ± 0.18	–	–	–
TOI-681	1.45 ± 0.25	1.51 ± 0.09	2.61 ± 0.13	–	–	–
TOI-746	0.84 ± 0.12	0.98 ± 0.06	7.9 ± 1.6	0.52 ± 0.06	−4.50 ± 0.05	0.60 ± 0.23
TOI-1213	0.93 ± 0.15	1.01 ± 0.06	12.0 ± 3.6	1.1 ± 0.2	–	–

Notes. We refer the reader to the final adopted parameters for each star presented in Tables A.2–A.6. $^{(a)}$Stellar mass inferred from $R_\star$ and spectroscopic $\log g_*$. $^{(b)}$Stellar mass estimated via empirical relations of Torres et al. (2010). $^{(c)}$System age estimated from inferred rotation period via empirical relations of Mamajek & Hillenbrand (2008). $^{(d)}$System age estimated from inferred $R'_{\rm HK}$ via empirical relations of Mamajek & Hillenbrand (2008). The ages derived from stellar rotation and activity are likely underestimated due to the stellar rotations likely being affected by the companions as discussed in Sect. 4.1.

Rubin 1992; Gelman et al. 2003; Ford 2006) is used to check the convergence of the chains. For each fit we use $2 \times n_{\rm parameters}$ walkers, or chains, and run until the fit passes the default convergence criteria for EXOFASTv2 that is described in Eastman et al. (2019). For each star we simultaneously fit the RVs and photometry and determine stellar parameters using the Modules for Experiments in Stellar Astrophysics (MESA) Isochrones & Stellar Tracks (MIST; Paxton et al. 2015; Choi et al. 2016; Dotter 2016) isochrones.

We place Gaussian priors on R_* and $T_{\rm eff}$ from the SED analysis described in Sect. 3.2 and do not fit the SED again within the EXOFASTv2 global model. We place Gaussian priors on [Fe/H] from the spectroscopic analysis described in Sect. 3.1. For TOI-681 we use the NGC 2516 cluster age discussed in Sect. 3.3 as a prior. We place upper boundaries on the companion radius for TOI-681 and TOI-1213 due to the grazing nature of their transits, which we discuss further in Sect. 3.4.2.

EXOFASTv2 inherently applies priors on the quadratic limb darkening by interpolating the Claret & Bloemen (2011) limb darkening models at each step in $\log g_*$, $T_{\rm eff}$, and [Fe/H]. We use the inherent EXOFASTv2 limb darkening fitting without applying priors on any filters for TOI-148, TOI-681, TOI-746, and TOI-1213. However, given TOI-587's high $T_{\rm eff}$ we disable the limb darkening table interpolation using the `noclaret` option in EXOFASTv2 and apply Gaussian priors of $u_1 = 0.15 \pm 0.1$ for the linear limb-darkening coefficient and $u_2 = 0.25 \pm 0.1$ for the quadratic limb-darkening coefficient for the TOI-587 TESS FFI lightcurve. To account for smearing in the 30-min TESS full frame exposures, we specify an exposure time of 30 min and average over 10 data points to integrate a model over the exposure time equivalent to a midpoint Riemann sum (Eastman et al. 2019).

Specific priors used for each EXOFASTv2 fit are displayed in Tables A.2–A.6 as well as the final results for both the host star and companion parameters. All other fitted and derived parameters from our EXOFASTv2 model have conservative physical boundaries that are detailed in Table 3 of Eastman et al. (2019), which also gives a thorough explanation of each parameter. The final EXOFASTv2 transit and RV Keplerian fits are displayed as the red lines in Figs. 1–5.

3.4.2. TOI-681 and TOI-1213 grazing transits

TOI-681 and TOI-1213 both have v-shaped light curves which suggests that their companions have grazing transits. In such cases where transiting companions have a grazing geometry there is a degeneracy between the companion radius and impact parameter of the transit and the upper limit of the companion radius is unconstrained by the light curve. For TOI-681 we find that the posterior distribution of both the companion radius and impact parameter are bimodal with the lower companion radius and impact parameter being favored. We show the unconstrained posterior distribution of the companion radius in Fig. 8. Given this clear bimodality and a more probable lower-radius solution both physically and statistically, we remodeled TOI-681 with very conservative boundaries of 0 and 5 $R_{\rm Jup}$ for the companion radius. We show the new companion radius posterior distribution in Fig. 8 that finds a clear peak at ∼1.5 $R_{\rm Jup}$.

The posterior distribution for the companion radius of TOI-1213 does not clearly favor the lower-radius solution, and the most probable solution is at a much larger radius than physically expected. We therefore put a tighter upper boundary of 3.0 $R_{\rm Jup}$ for TOI-1213 when remodeling the system based on the physical limit of nondetections of the occultations in the TESS light curve. From our EXOFASTv2 model we find an eclipse impact parameter of $0.403^{+0.041}_{-0.027}$ showing the system should be aligned to see an occultation in the lightcurve if it is within the TESS detection limits. As displayed in Fig. 9 we do not find any occultations of TOI-1213b within the precision of the TESS light curve, which allows us to put an upper limit on the occultation depth and thus an upper limit on the companion radius. The lower panel of Fig. 9 shows the first occultation and displays a box model of an occultation with a depth equal to the standard deviation (1725 ppm) of the TESS data during

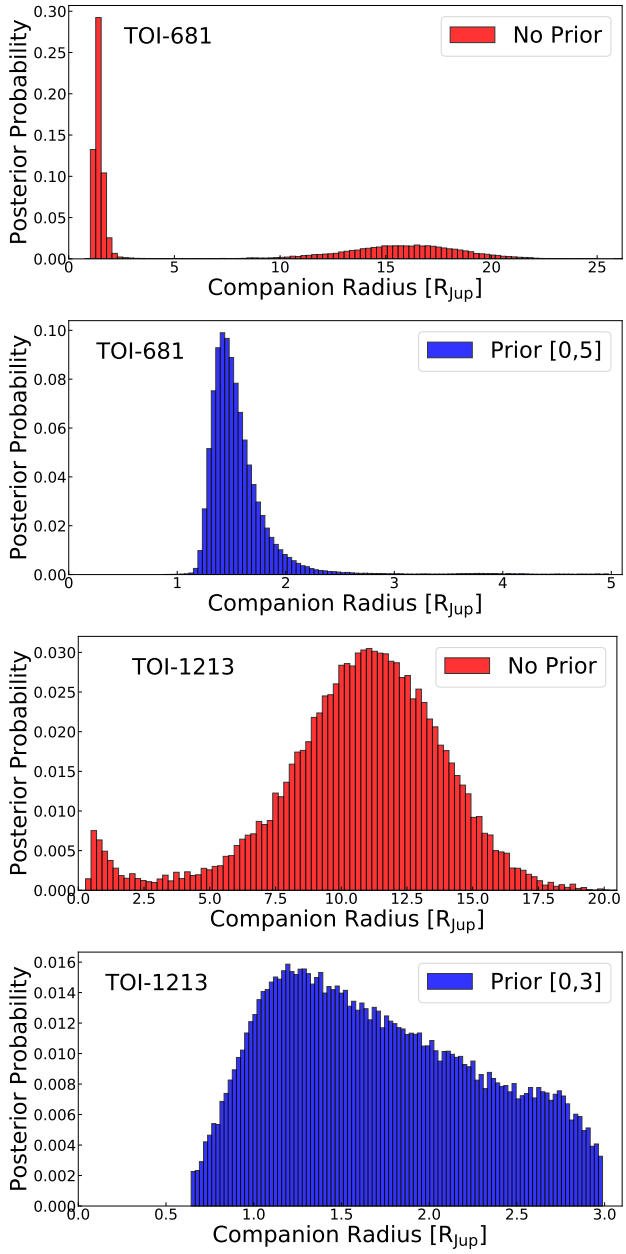

Fig. 8. EXOFASTv2 posterior distributions of the companion radii without (red) and with (blue) upper limits on the companion radius for TOI-681 and TOI-1213 as described in Sect. 3.4.2.

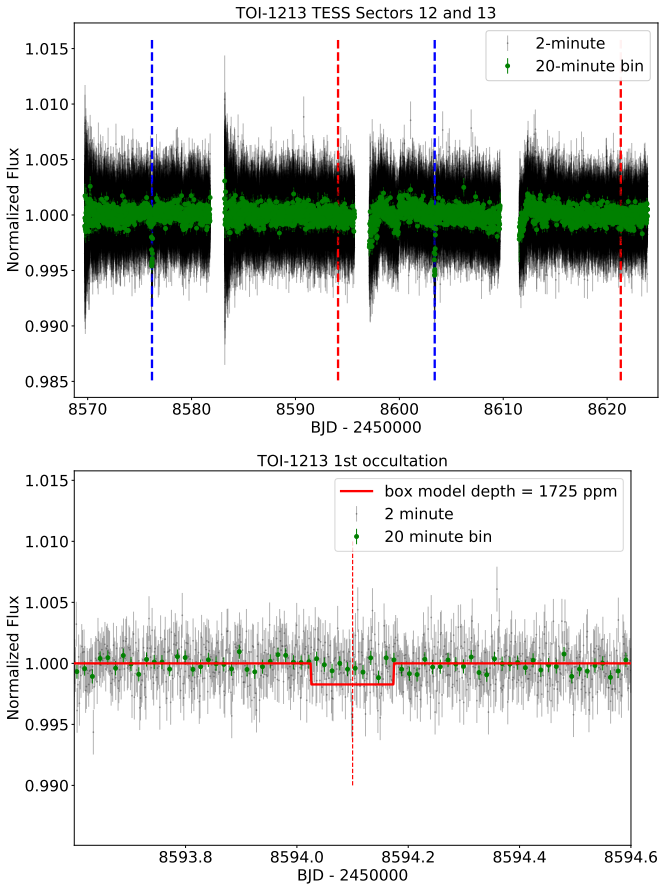

Fig. 9. *Top*: full light curve of TOI-1213 for TESS sectors 12 and 13. The blue dashed vertical lines display the times of transit and the red dashed vertical lines show the expected occultation times which we determined to be at a phase of 0.6581. *Bottom*: zoom in of the time where the first occultation of TOI-1213 should occur with a box model with a depth equal to the standard deviation of the TESS photometry during the total eclipse duration (0.149 days) calculated from our EXOFASTv2 model.

the total eclipse duration ($0.149^{+0.015}_{-0.014}$ days) calculated from our EXOFASTv2 model. We set this standard deviation of 1725 ppm as our detection limit and the lower limit of the occultation depth. To turn this occultation depth limit into an upper limit on the companion radius, we obtained simulated PHOENIX spectra (Husser et al. 2013) of a G6V star for TOI-1213 and M7.5V for TOI-1213b (from our calculated mass of 97.5 $M_{\rm Jup}$) and integrated the total flux of each spectrum over the TESS bandpass of 600–1000 nm. We then multiply this total flux of the modeled G6V star by the area of TOI-1213 $\pi {R_*}^2$. The companion radius can then be computed by setting the occultation depth to the TESS precision:

$$\mathrm{Depth_{occ}} = \frac{\mathrm{Flux_b}\pi R_\mathrm{b}^2}{\mathrm{Flux_A}\pi R_A^2}. \quad (1)$$

With a lower limit on occultation of 1725 ppm, we find an upper limit on the companion radius of 3.00 $R_{\rm Jup}$. We set 3.0 $R_{\rm Jup}$ as the upper limit on TOI-1213b and display the companion radius with and without boundaries in Fig. 8.

4. Discussion

The five transiting companions analyzed here have masses around the hydrogen-burning mass limit, the upper boundary of brown dwarfs and lower boundary of main sequence stars, which is generally adopted as 80 $M_{\rm Jup}$ (e.g., Marcy & Butler 2000; Grether & Lineweaver 2006). However, this border depends on initial formation conditions including the initial radius of the object, the efficiency of convection in the outermost layers, opacity, metallicity, and the initial abundance of deuterium (e.g., Chabrier & Baraffe 1997; Baraffe et al. 2002). Dieterich et al. (2018) summarizes previous model predictions for the stellar-substellar boundary which range from 73.3–96.4 $M_{\rm Jup}$ (e.g., Burrows et al. 2001), whose predictions differ from observed populations (e.g., Dieterich et al. 2014) and differ from the ∼70 $M_{\rm Jup}$ boundary estimate by Dupuy & Liu (2017) using astrometric masses of ultracool binaries.

This brown dwarf and stellar boundary is important as small changes in mass can cause vastly different lives for these objects,

where low-mass M-dwarfs may burn hydrogen for up to trillions of years (e.g., Adams & Laughlin 1997) compared to brown dwarfs that will only have a short-lived deuterium burning stage of less than a billion years (e.g., Spiegel et al. 2011) before cooling and shrinking. The exact population these five objects belong to is uncertain, but we can put them into context with other transiting brown dwarfs and very low-mass stars as discussed in Sect. 4.2. We first explore the possible tidal effects on these individual systems in Sect. 4.1.

4.1. Tidal circularization and spin-orbit synchronization

The gravitational and tidal interactions between a star and a close-in orbiting companion (another star, brown dwarf, or planet) have varying effects on the rotation, orbit, and momentum axes of the system. In terms of timescales, the first effect that may be induced is spin-orbit synchronization, or tidal locking, where the stellar rotation period and orbital period become equal from tidal torques (e.g., Zahn 1977; Zahn & Bouchet 1989; Witte & Savonije 2002; Mazeh 2008). A system with an eccentric orbit can reach a tidally locked state when the stellar rotation period becomes equal to the equilibrium rotation period, which can be predicted by tidal models (Fleming et al. 2019). A star's rotation period is generally expected to reduce over time from magnetic braking (Skumanich 1972); however, this affect may be slowed down due to tidal torques (e.g., Verbunt & Zwaan 1981; Fleming et al. 2018, 2019). On longer timescales and particularly for short orbital periods (e.g., $P_{\rm orb} \lesssim 10$ days) the orbital eccentricity may be damped and the orbit may become circular (e.g., tidal circularization, Goldreich & Soter 1966; Hut 1981; Adams & Laughlin 2006). Evolution of the system's obliquity, or the angle between the stellar spin axis and the orbital axis occurs even more slowly than eccentricity dampening (e.g., Hut 1981; Winn et al. 2005; Barker & Ogilvie 2009). Here we examine possible tidal effects including eccentricity dampening or circularization, stellar rotation spin up, and spin-orbit synchronization of the brown dwarf and low-mass star systems presented in this work.

From our spectroscopic analysis we find a $v \sin i_* = 10.1 \pm 0.1$ km s^{-1} for TOI-148, which is on the upper end of $v \sin i_*$ distributions for stars of similar mass (e.g., Robles et al. 2008), indicating TOI-148's stellar rotation period may be affected by tidal torques with its companion. With this $v \sin i_*$ we put an upper limit on the stellar rotation period ($P_{\rm rot} \leq 2\pi R_*/v \sin i_*$) of 5.97 ± 0.47 days for TOI-148, which is smaller than expected given its older age of 7.7 ± 3.7 Gyr in comparison to other rotational periods of older stars with similar masses (e.g., Lorenzo-Oliveira et al. 2019). Additionally the upper limit of the stellar rotation period is less than one day larger than the orbital period of 4.87 days for TOI-148b, suggesting that TOI-148 may be close to a tidally locked state. We find the eccentricity of TOI-148 $e = 0.005^{+0.006}_{-0.004}$ to be insignificant (using the significance test from Lucy & Sweeney (1971) we find $P(e > 0) = 0.63$, which fails the 5% significance level) also suggesting TOI-148 has undergone tidal circularization.

TOI-681 is relatively hot ($T_{\rm eff} = 7440^{+150}_{-140}$ K) and fast rotating ($P_{\rm rot}/\sin i = 2.61 \pm 0.13$ days) star, which can create enhanced magnetic fields from spin-orbit tidal synchronization for short period systems and has been thought to cause inflated radii of similar low-mass companions (e.g., Chabrier et al. 2007; Mazeh 2008). However, given its relatively long period of 15.78 days and young 0.170 ± 0.025 Gyr age TOI-681b is unlikely to have reached spin-orbit synchronization. TOI-587 is also a young 0.2 ± 0.1 Gyr star that is unlikely to have undergone spin-orbit synchronization with $P_{\rm rot}/\sin i = 3.02 \pm 0.18$ days and $P_{\rm orb} = 8.04$ days.

TOI-746 is an older $6.5^{+4.3}_{-3.9}$ Gyr star with a companion on a moderately eccentric $e = 0.199 \pm 0.003$ orbit. As discussed, tidal torques can drive a star's rotation rate toward a tidally locked state where the tidal torques fix the rotation period $P_{\rm rot}$ to the equilibrium rotation period $P_{\rm eq}$. Tidal models can predict $P_{\rm eq}$ including the "constant phase lag" (CPL; Ferraz-Mello et al. 2008; Heller et al. 2011) equilibrium tidal model. Following Barnes (2017) and Fleming et al. (2019) the CPL model permits a 1:1 and 3:2 spin-orbit state by:

$$P_{\rm eq}^{\rm CPL} = \begin{cases} P_{\rm eq} \text{ if } e < \sqrt{1/19} \\ \frac{2}{3} P_{\rm eq} \text{ if } e \geq \sqrt{1/19}. \end{cases} \quad (2)$$

Using the second case we find $P_{\rm eq} = 7.32$ days for TOI-746 and with an upper limit on the rotation period of $P_{\rm rot}/\sin i = 7.9 \pm 1.6$ days TOI-746 may be in a supersychronous 3:2 spin-orbit state. We also consider the system may be in a pseudo-synchronous rotation state (Hut 1981) that approximates spin-orbit synchronization around the time of periastron. Zimmerman et al. (2017) explored possible pseudosynchronization for heartbeat binary stars with *Kepler* lightcurves but found generally that their sample clustered around $\frac{3}{2}$ times the pseudosynchronization period indicating that they have plateaued prematurely in their synchronization. We roughly estimate this using Kepler's third law to determine what the period would be if the companion was in a circular orbit at the periastron distance:

$$P_{\rm peri} = P_{\rm orb}(1 - e)^{3/2}. \quad (3)$$

Assuming this circular orbit at periastron we find $P_{\rm peri} = 7.88 \pm 0.05$ days which is very similar to the upper limit of the rotation period suggesting TOI-746 may be in a pseudo-synchronous rotation at periastron.

TOI-1213 is also relatively older $5.3^{+4.2}_{-3.4}$ Gyr star with a companion on an eccentric $e = 0.498^{+0.003}_{-0.002}$ orbit. We find $P_{\rm eq} = 18.14$ days for TOI-1213, and with $P_{\rm rot}/\sin i = 12.0 \pm 3.6$ days TOI-1213 does not appear to have spin-orbit synchronization. However, assuming a circular orbit at periastron we find $P_{\rm peri} = 9.64 \pm 0.09$ days, which is within uncertainties of the upper limit of the stellar rotation period suggesting TOI-1213 may be in a pseudo-synchronous rotation at periastron.

4.2. Discoveries in context with transiting brown dwarfs and very low-mass stars

Here we place these five transiting companions into context by comparing them with other very low-mass stars and brown dwarfs using transiting brown dwarfs from the list compiled by Carmichael et al. (2021). We also include 21 low-mass stars with masses between 80 and 150 $M_{\rm Jup}$ from the list compiled by Mireles et al. (2020). We exclude the brown dwarf binary system from Stassun et al. (2006) and triple system from Triaud et al. (2020) so as only to focus on transiting companions. We also exclude brown dwarfs and low-mass stars known to transit white dwarfs (e.g., Parsons et al. 2012a,b,c). We add the three recent transiting brown dwarf discoveries of GPX-1b (Benni et al. 2021), TOI-263b (Palle et al. 2021), and TOI-1278b (Artigau et al. 2021). This includes a total of 54 transiting companions in the mass range of 13–150 $M_{\rm Jup}$ presented in Table 4.

Table 4. Published 13–150 $M_{\rm Jup}$ transiting companions as of June 2021.

Name	M_2 [$M_{\rm Jup}$]	R_2 [$R_{\rm Jup}$]	P [days]	ecc	M_1 [$M_\odot$]	R_1 [$R_\odot$]	$T_{\rm eff}$[K]	[Fe/H]	Reference
HATS-70b	$12.9^{+1.8}_{-1.6}$	$1.38^{+0.08}_{-0.07}$	1.89	<0.18	1.78 ± 0.12	$1.88^{+0.06}_{-0.07}$	7930^{+630}_{-820}	$0.04^{+0.10}_{-0.11}$	(1)
TOI-1278b	18.5 ± 0.5	$1.09^{+0.24}_{-0.20}$	14.48	0.013 ± 0.004	0.54 ± 0.02	0.57 ± 0.01	3799 ± 42	-0.01 ± 0.28	(2)
GPX-1b	19.7 ± 1.6	1.47 ± 0.10	1.74	0.000 ± 0.000	1.68 ± 0.10	1.56 ± 0.10	7000 ± 200	0.35 ± 0.10	(3)
Kepler-39b	$20.1^{+1.3}_{-1.2}$	$1.24^{+0.09}_{-0.10}$	21.09	0.112 ± 0.057	$1.29^{+0.06}_{-0.07}$	1.40 ± 0.10	6350 ± 100	0.10 ± 0.14	(4)
CoRoT-3b	21.7 ± 1.0	1.01 ± 0.07	4.26	0 (fixed)	1.37 ± 0.09	1.56 ± 0.09	6740 ± 140	-0.02 ± 0.06	(5)
KELT-1b	27.4 ± 0.9	$1.12^{+0.04}_{-0.03}$	1.22	$0.010^{+0.010}_{-0.007}$	1.33 ± 0.06	1.47 ± 0.04	6516 ± 49	0.05 ± 0.08	(6)
NLTT 41135b	$33.7^{+2.8}_{-2.6}$	$1.13^{+0.27}_{-0.17}$	2.89	<0.02	$0.19^{+0.03}_{-0.02}$	$0.21^{+0.02}_{-0.01}$	3230 ± 130	-0.25 ± 0.25	(7)
WASP-128b	37.2 ± 0.8	0.94 ± 0.02	2.21	<0.007	1.16 ± 0.04	1.15 ± 0.02	5950 ± 50	0.01 ± 0.12	(8)
CWW 89Ab	$39.2^{+0.9}_{-1.1}$	0.94 ± 0.02	5.29	0.189 ± 0.002	1.10 ± 0.04	1.03 ± 0.02	5755 ± 49	0.20 ± 0.09	(9) (10)
KOI-205b	39.9 ± 1.0	0.81 ± 0.02	11.72	<0.031	0.93 ± 0.03	0.84 ± 0.02	5237 ± 60	0.14 ± 0.12	(11)
TOI-1406b	$46.0^{+2.6}_{-2.7}$	0.86 ± 0.03	10.57	$0.026^{+0.013}_{-0.010}$	$1.18^{+0.08}_{-0.09}$	1.35 ± 0.03	6290 ± 100	-0.08 ± 0.09	(12)
EPIC 212036875b	52.3 ± 1.9	0.87 ± 0.02	5.17	0.132 ± 0.004	$1.29^{+0.07}_{-0.06}$	1.50 ± 0.03	6238^{+59}_{-60}	0.01 ± 0.10	(10) (13)
TOI-503b	53.7 ± 1.2	$1.34^{+0.26}_{-0.15}$	3.68	0 (fixed)	1.80 ± 0.06	$1.70^{+0.05}_{-0.04}$	7650^{+140}_{-160}	$0.30^{+0.08}_{-0.09}$	(14)
TOI-852b	$53.7^{+1.4}_{-1.3}$	0.83 ± 0.04	4.95	$0.004^{+0.004}_{-0.003}$	$1.32^{+0.05}_{-0.04}$	1.71 ± 0.04	5768^{+84}_{-81}	0.33 ± 0.09	(15)
AD 3116b	54.2 ± 4.3	1.02 ± 0.28	1.98	0.146 ± 0.024	0.28 ± 0.02	0.29 ± 0.08	3184 ± 29	0.16 ± 0.10	(16)
CoRoT-33b	$59.0^{+1.8}_{-1.7}$	1.10 ± 0.53	5.82	0.070 ± 0.002	0.86 ± 0.04	$0.94^{+0.14}_{-0.08}$	5225 ± 80	0.44 ± 0.10	(17)
RIK 72b	$59.2^{+6.8}_{-6.7}$	3.10 ± 0.31	97.76	$0.108^{+0.012}_{-0.006}$	0.44 ± 0.04	0.96 ± 0.10	3349 ± 142	0.00 ± 0.10	(18)
TOI-811b	$59.9^{+13.0}_{-8.6}$	1.26 ± 0.06	25.17	0.509 ± 0.075	$1.32^{+0.05}_{-0.07}$	$1.27^{+0.06}_{-0.09}$	6107 ± 77	$0.40^{+0.07}_{-0.09}$	(15)
TOI-263b	61.6 ± 4.0	0.91 ± 0.07	0.56	$0.017^{+0.009}_{-0.010}$	0.44 ± 0.04	0.44 ± 0.03	3471 ± 33	0.00 ± 0.10	(19)
KOI-415b	62.1 ± 2.7	$0.79^{+0.12}_{-0.07}$	166.79	0.689 ± 0.000	0.94 ± 0.06	$1.25^{+0.15}_{-0.10}$	5810 ± 80	-0.24 ± 0.11	(20)
WASP-30b	62.5 ± 1.2	$0.95^{+0.03}_{-0.02}$	4.16	0 (fixed)	$1.25^{+0.03}_{-0.04}$	1.39 ± 0.03	6202^{+42}_{-51}	$0.08^{+0.07}_{-0.05}$	(21)
LHS 6343c	62.7 ± 2.4	0.83 ± 0.02	12.71	0.056 ± 0.032	0.37 ± 0.01	0.38 ± 0.01	3130 ± 20	0.04 ± 0.08	(22)
CoRoT-15b	63.3 ± 4.1	$1.12^{+0.30}_{-0.15}$	3.06	0 (fixed)	1.32 ± 0.12	$1.46^{+0.31}_{-0.14}$	6350 ± 200	0.10 ± 0.20	(23)
TOI-569b	$64.1^{+1.9}_{-1.4}$	0.75 ± 0.02	6.56	$0.002^{+0.002}_{-0.001}$	1.21 ± 0.05	1.48 ± 0.03	5768^{+110}_{-92}	$0.29^{+0.09}_{-0.08}$	(12)
EPIC 201702477b	66.9 ± 1.7	0.76 ± 0.07	40.74	0.228 ± 0.003	0.87 ± 0.03	0.90 ± 0.06	5517 ± 70	-0.16 ± 0.05	(24)
LP261-75b	68.1 ± 2.1	0.90 ± 0.01	1.88	<0.007	0.30 ± 0.01	0.31 ± 0.00	3100 ± 50	...	(25)
NGTS-7Ab	$75.5^{+3.0}_{-13.7}$	$1.38^{+0.13}_{-0.14}$	0.68	0 (fixed)	0.24 ± 0.03	0.61 ± 0.06	3359^{+106}_{-89}	0.00 ± 0.10	(26)
KOI-189b	78.6 ± 3.5	1.00 ± 0.02	30.36	0.275 ± 0.004	0.76 ± 0.05	0.73 ± 0.02	4952 ± 40	-0.12 ± 0.10	(27)
TOI-148b	$77.1^{+5.8}_{-4.6}$	$0.81^{+0.05}_{-0.06}$	4.87	$0.005^{+0.006}_{-0.004}$	$0.97^{+0.12}_{-0.09}$	1.20 ± 0.07	5990 ± 140	-0.24 ± 0.25	This work
TOI-587b	$81.1^{+7.1}_{-7.0}$	$1.32^{+0.07}_{-0.06}$	8.04	$0.051^{+0.049}_{-0.036}$	2.33 ± 0.12	2.01 ± 0.09	9800 ± 200	$0.08^{+0.11}_{-0.12}$	This work
TOI-746b	$82.2^{+4.9}_{-4.4}$	$0.95^{+0.09}_{-0.06}$	10.98	0.199 ± 0.003	$0.94^{+0.09}_{-0.08}$	$0.97^{+0.04}_{-0.03}$	5690 ± 140	-0.02 ± 0.23	This work
EBLM J0555-57Ab	87.9 ± 4.0	$0.82^{+0.13}_{-0.06}$	7.76	0.089 ± 0.004	1.18 ± 0.08	$1.00^{+0.14}_{-0.07}$	6386 ± 124	-0.04 ± 0.14	(28)
TOI-681b	$88.7^{+2.5}_{-2.3}$	$1.52^{+0.25}_{-0.15}$	15.78	$0.093^{+0.022}_{-0.019}$	$1.54^{+0.06}_{-0.05}$	1.47 ± 0.04	7440^{+150}_{-140}	-0.08 ± 0.05	This work
OGLE-TR-123b	89.0 ± 11.5	1.29 ± 0.09	1.80	0 (fixed)	1.29 ± 0.26	1.55 ± 0.10	6700 ± 300	...	(29)
TOI-694b	89.0 ± 5.3	1.11 ± 0.02	48.05	0.521 ± 0.002	$0.97^{+0.05}_{-0.04}$	1.00 ± 0.01	5496^{+87}_{-81}	0.21 ± 0.08	(30)
KOI-607b	$95.1^{+3.3}_{-3.4}$	$1.09^{+0.09}_{-0.06}$	5.89	0.395 ± 0.009	0.99 ± 0.05	0.92 ± 0.03	5418^{+87}_{-85}	$0.38^{+0.07}_{-0.09}$	(10)
J1219-39b	$95.4^{+1.9}_{-2.5}$	$1.14^{+0.07}_{-0.05}$	6.76	0.055 ± 0.000	0.83 ± 0.03	$0.81^{+0.04}_{-0.02}$	5412^{+81}_{-65}	-0.21 ± 0.07	(21)
OGLE-TR-122b	96.3 ± 9.4	$1.17^{+0.20}_{-0.13}$	7.27	0.205 ± 0.008	0.98 ± 0.14	$1.05^{+0.20}_{-0.09}$	5700 ± 300	0.15 ± 0.36	(31)
TOI-1213b	$97.5^{+4.4}_{-4.2}$	$1.66^{+0.78}_{-0.55}$	27.22	$0.498^{+0.003}_{-0.002}$	$0.99^{+0.07}_{-0.06}$	0.99 ± 0.04	5590 ± 150	$0.25^{+0.13}_{-0.14}$	This work
K2-76b	98.7 ± 2.0	$0.89^{+0.03}_{-0.05}$	11.99	$0.255^{+0.007}_{-0.006}$	0.96 ± 0.03	$1.17^{+0.03}_{-0.06}$	5747^{+64}_{-70}	0.01 ± 0.04	(32)
CoRoT 101 186 644	100.5 ± 11.5	$1.01^{+0.06}_{-0.25}$	20.68	0.402 ± 0.006	1.20 ± 0.20	1.07 ± 0.07	6090 ± 200	0.20 ± 0.20	(33)
J2343+29Ab	102.7 ± 7.3	1.24 ± 0.07	16.95	$0.161^{+0.002}_{-0.003}$	0.86 ± 0.10	$0.85^{+0.05}_{-0.06}$	5150^{+90}_{-60}	0.10 ± 0.14	(34)
EBLM J0954-23Ab	$102.8^{+6.0}_{-5.9}$	0.98 ± 0.17	7.58	0.042 ± 0.001	1.17 ± 0.08	1.23 ± 0.17	6406 ± 124	-0.01 ± 0.14	(28)
KOI-686b	103.4 ± 5.1	1.22 ± 0.04	52.51	0.556 ± 0.004	0.98 ± 0.07	1.04 ± 0.03	5834 ± 100	-0.06 ± 0.13	(27)
TIC 220568520b	107.2 ± 5.2	1.25 ± 0.02	18.56	0.096 ± 0.003	1.03 ± 0.04	1.01 ± 0.01	5589 ± 81	0.26 ± 0.07	(30)
HATS551-016B	$114.7^{+5.2}_{-6.3}$	$1.46^{+0.03}_{-0.04}$	2.05	0.080 ± 0.020	$0.97^{+0.05}_{-0.06}$	$1.22^{+0.02}_{-0.03}$	6420 ± 90	-0.60 ± 0.06	(35)
OGLE-TR-106b	121.5 ± 22.0	1.76 ± 0.17	2.54	0.000 ± 0.020	...	1.31 ± 0.09	...	...	(36)
EBLM J1431-11Ab	$126.9^{+3.8}_{-3.9}$	$1.45^{+0.07}_{-0.05}$	4.45	0 (fixed)	1.20 ± 0.06	$1.11^{+0.04}_{-0.03}$	6161 ± 124	0.15 ± 0.14	(28)
HAT-TR-205-013B	129.9 ± 10.5	1.62 ± 0.06	2.23	0.012 ± 0.021	1.04 ± 0.13	1.28 ± 0.04	6295^{+245}_{-335}	...	(37)
TIC 231005575b	134.1 ± 3.1	1.50 ± 0.03	61.78	$0.298^{+0.004}_{-0.001}$	1.04 ± 0.04	0.99 ± 0.05	5500 ± 85	-0.44 ± 0.06	(38)
HATS551-021B	$138.2^{+14.7}_{-5.2}$	$1.53^{+0.06}_{-0.08}$	3.64	0.060 ± 0.020	1.10 ± 0.10	$1.20^{+0.08}_{-0.01}$	6670 ± 220	-0.40 ± 0.10	(35)
EBLM J2017+02Ab	$142.2^{+6.6}_{-6.7}$	$1.49^{+0.13}_{-0.10}$	0.82	0 (fixed)	1.10 ± 0.07	$1.20^{+0.08}_{-0.05}$	6161 ± 124	-0.07 ± 0.14	(28)
KIC 1571511B	148.1 ± 0.5	$1.74^{+0.00}_{-0.01}$	14.02	0.327 ± 0.003	$1.26^{+0.04}_{-0.03}$	1.34 ± 0.01	6195 ± 50	0.37 ± 0.08	(39)
WTS 19g-4-02069B	149.8 ± 6.3	1.69 ± 0.06	2.44	0 (fixed)	0.53 ± 0.02	0.51 ± 0.01	3300 ± 140	...	(40)

Notes. The brown dwarf binary system from Stassun et al. (2006), triple system from Triaud et al. (2020), and white dwarf companions are not included.

References. (1) Zhou et al. (2019); (2) Artigau et al. (2021); (3) Benni et al. (2021); (4) Bonomo et al. (2015); (5) Deleuil et al. (2008); (6) Siverd et al. (2012); (7) Irwin et al. (2010); (8) Hodžić et al. (2018); (9) Nowak et al. (2017); (10) Carmichael et al. (2019); (11) Díaz et al. (2013); (12) Carmichael et al. (2020); (13) Persson et al. (2019); (14) Šubjak et al. (2020); (15) Carmichael et al. (2021); (16) Gillen et al. (2017); (17) Csizmadia et al. (2015); (18) David et al. (2019); (19) Palle et al. (2021); (20) Moutou et al. (2013); (21) Triaud et al. (2013); (22) Johnson et al. (2011); (23) Bouchy et al. (2011); (24) Bayliss et al. (2017); (25) Irwin et al. (2018); (26) Jackman et al. (2019); (27) Díaz et al. (2014); (28) von Boetticher et al. (2019); (29) Pont et al. (2006); (30) Mireles et al. (2020); (31) Pont et al. (2005b); (32) Shporer et al. (2017); (33) Tal-Or et al. (2013); (34) Chaturvedi et al. (2016); (35) Zhou et al. (2014); (36) Pont et al. (2005a); (37) Beatty et al. (2007); (38) Gill et al. (2020); (39) Ofir et al. (2012); (40) Nefs et al. (2013).

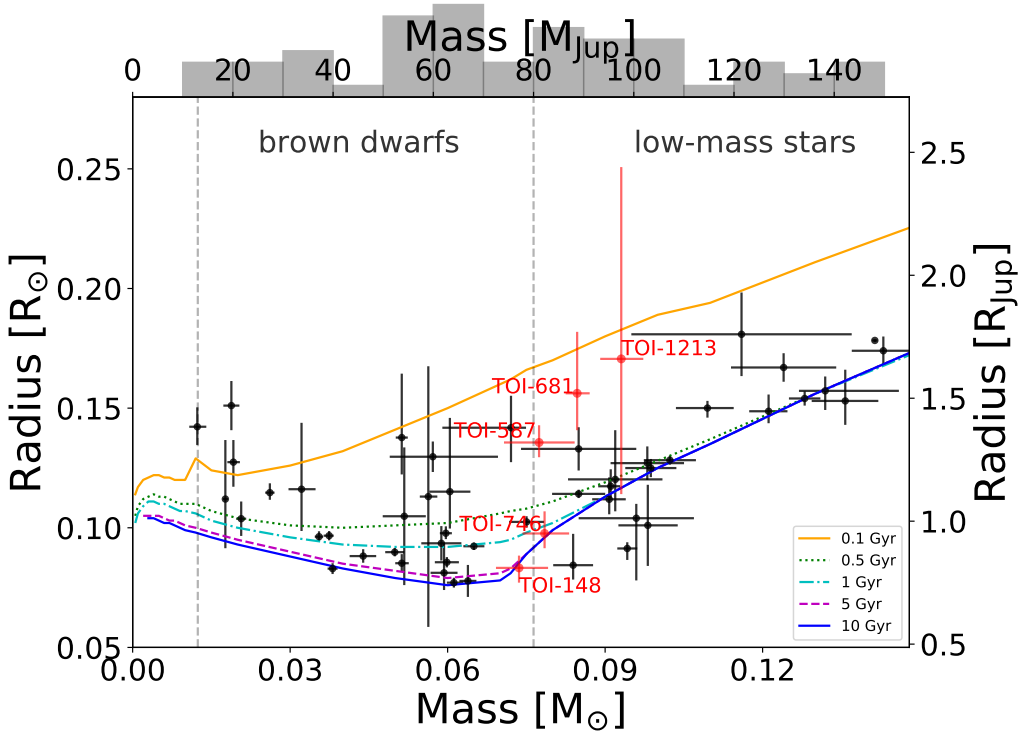

Fig. 10. Radius-mass diagram for the 54 brown dwarfs and low-mass stars presented in Table 4. The five companions presented in this work are highlighted in red. The gray vertical dashed lines display the 13 and 80 $M_{\rm Jup}$ approximate boundaries of the brown dwarf regime. The colored lines display isochrone models from Baraffe et al. (2003, 2015) for low mass stars and substellar objects at solar metallicity with ages of 0.1, 0.5, 1, 5, and 10 Gyr. The histogram at the top displays relative occurrence of these transiting objects. We note the brown dwarf RIK 72b is not shown because its radius is 3.1 $R_{\rm Jup}$.

4.2.1. 13-150 $M_{\rm Jup}$ transiting companion radius-mass relationship

Figure 10 places the five objects studied here in the radius-mass diagram with transiting brown dwarfs and low-mass stars with masses up to 150 $M_{\rm Jup}$. We also plot the theoretical isochrones for solar metallicity at ages 0.1, 0.5, 1, 5, and 10 Gyr from Baraffe et al. (2003, 2015). Theoretical isochrones for low-mass stars and brown dwarfs (e.g., Baraffe et al. 2003, 2015) show the age of the object should affect its radius for a particular mass, with older objects having smaller radii. This is particularly true for brown dwarfs that do not have the long-term outward pressure of hydrogen fusion to balance out the crush of gravity. Using well-defined ages Carmichael et al. (2021) displayed a clear contrast between the radii of an old and a young brown dwarf; further systems with well-characterized ages are crucial to test this age-radius effect.

We derive young ages for TOI-681 (0.170 ± 0.025 Gyr from cluster membership) and TOI-587 (0.2 ± 0.1 Gyr from MIST isochrone stellar modeling of the hot A star) and see relatively enlarged radii for both of these objects. However, TOI-681b displays a slightly grazing transit and therefore the radius may be overestimated. TOI-681's age is notably close to the Pleiades cluster whose brown dwarf and very low-mass star candidates were spectroscopically classified as late M dwarfs (e.g., Dahm 2015).

As discussed in Sect. 3.4.2 TOI-1213b's radius is not well constrained from the grazing transit geometry and possibly overestimated given its age of $5.3^{+4.2}_{-3.4}$ Gyr. We find an older 7.7 ± 3.7 Gyr age for TOI-148 and with $R_{\rm b} = 0.81^{+0.05}_{-0.06}\,R_{\rm Jup}$ TOI-148b has one of the smallest radii among 13–150 $M_{\rm Jup}$ transiting companions. We also find an older $6.5^{+4.3}_{-3.9}$ Gyr age for TOI-746 and a relatively small $0.95^{+0.09}_{-0.06}\,R_{\rm Jup}$ companion radius.

The histogram on top of Fig. 10 displays relative occurrence of these transiting objects. Currently more massive brown dwarfs seem to have a slightly higher occurrence than less massive brown dwarfs. However, we note this is an incomplete sample and more systems are needed to understand the occurrence of these objects. Additionally we note that there may be a bias of not publishing low-mass stars as many current transit and RV research teams emphasize lower mass companion discoveries.

4.2.2. 13–150 $M_{\rm Jup}$ transiting companion eccentricity distribution.

By interpreting the eccentricity distribution of known brown dwarf candidate companions around FGK-type stars, many of which only had lower-mass estimates ($M_{\rm BD} \sin i$), Ma & Ge (2014) suggested that brown dwarfs could be split at ~42.5 $M_{\rm Jup}$. Brown dwarfs below 42.5 $M_{\rm Jup}$ may primarily form in the protoplanetary disk through core-accretion or disk gravitational instability and brown dwarfs above this mass may dominantly form like a stellar binary through molecular cloud fragmentation. This was suggested because lower-mass brown dwarfs showed a trend in their eccentricity distribution with lower maximum eccentricity with increasing mass, consistent with eccentricity scattering with other objects formed in the disk (e.g., 'planet-planet scattering', Rasio & Ford 1996; Chatterjee et al. 2008; Ford & Rasio 2008). Where higher-mass brown dwarfs showed more diverse eccentricities similar to that of stellar binaries (Ma & Ge 2014). This trend was again analyzed for known brown dwarf companions by Grieves et al. (2017) who found an overall similar distribution. Additionally, Kiefer et al. (2021) found the eccentricity distribution for brown dwarfs and low-mass M-dwarf companions around FGK stars at less than 60 pc of the Sun with a true mass measured to match that of Ma & Ge (2014).

We analyze the eccentricity distribution for transiting brown dwarfs and low-mass stars up to 150 $M_{\rm Jup}$ in Fig. 11. Although the higher-mass brown dwarfs and low-mass stars display a larger range in eccentricities, the sample size is still too small to make a claim that these represent two separate populations. The symbols in Fig. 11 are colored by period, and as expected the companions with the highest eccentricities have relatively longer orbital periods.

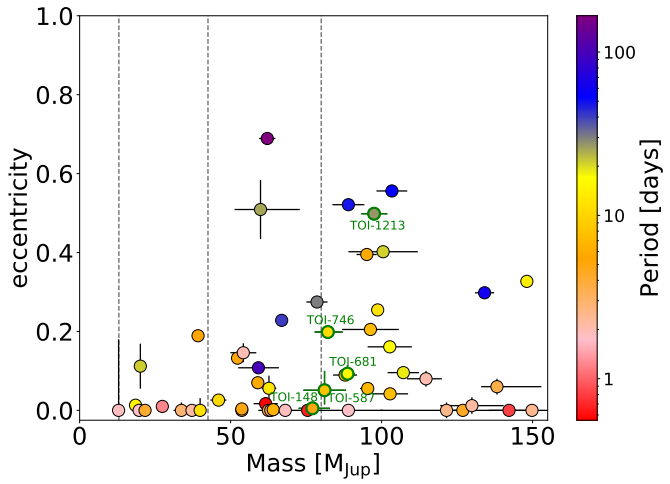

Fig. 11. Eccentricity and mass for transiting brown dwarfs and low-mass stellar companions. The color of each circle denotes the period. Transiting companions presented in this work have green edges and error bars. The vertical dashed lines are on the masses of 13, 42.5, and 80 M_{Jup}.

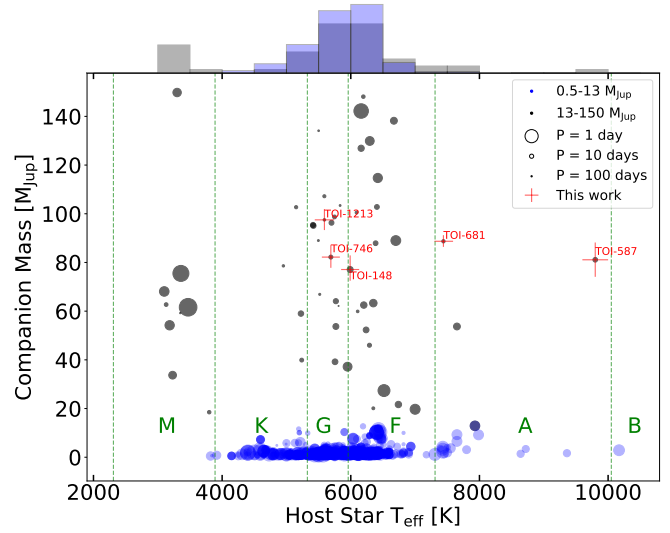

Fig. 12. Companion mass and host star effective temperature T_{eff} for transiting brown dwarfs and low-mass stellar companions (gray circles) with the five new companions of this work shown with red error bars. We also display giant planets that have both RV and transit data from the NASA exoplanet archive (https://exoplanetarchive.ipac.caltech.edu) (1089 giant planets) with blue circles. The circles are inversely sized by the companion period to highlight a higher proportion of brown dwarfs and low-mass stars in close orbit around F dwarfs. The histograms at the top display the number of relative companions in 500 K T_{eff} bins. The vertical dashed green lines display approximate T_{eff} borders of stellar types.

4.2.3. 13–150 M_{Jup} transiting companion host stars

We review the host star effective temperature and stellar type of transiting brown dwarfs and low-mass stars in Fig. 12. G and F-type host stars are the most common while there are only four hotter K-type stars hosting a transiting companion in the mass range 13–150 M_{Jup}. As noted by Carmichael et al. (2020) we see a relatively large percentage of transiting BDs with M dwarf host stars, which is in contrast to hot Jupiters that have a relatively smaller percentage of M dwarf host stars. TOI-587 is the hottest main-sequence host star of a transiting brown dwarf or

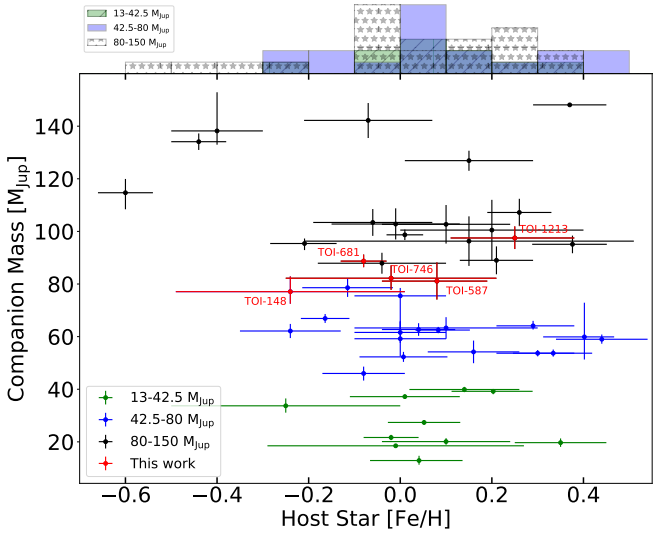

Fig. 13. Companion mass and host star metallicity [Fe/H] for transiting brown dwarfs and low-mass stellar companions. We split the companions between 13–42.5, 42.5–80, and 80–150 M_{Jup} to visualize possible metallicity differences between low-mass and high-mass brown dwarfs and low-mass stars. The histograms at the top display the number of companions in 0.1 dex [Fe/H] bins for these mass ranges.

low-mass star below 150 M_{Jup} with a $T_{eff} = 9800^{+200}_{-200}$ K. From the most recent table[4] of mean dwarf star effective temperatures by Pecaut & Mamajek (2013) we find stellar types of F9.5V for TOI-148, A0V for TOI-587, A9V for TOI-681, G4V for TOI-746, and G6V for TOI-1213.

In Fig. 12, following Bouchy et al. (2011), the symbol size is inversely proportional to the companion orbital period in order to highlight the higher proportion of brown dwarfs and low-mass stars found in close orbit around F dwarfs compared to those around G dwarfs. A plausible conjecture is that G dwarfs may have engulfed their close-in brown-dwarf companions while F dwarfs, which undergo less magnetic braking (e.g., Sadeghi Ardestani et al. 2017), would have preserved them (Guillot et al. 2014). The two companions orbiting G dwarfs from this study, TOI-746 and TOI-1213, are both relatively long-period (10.98 days and 27.22 days, respectively) and eccentric (see Fig. 11), indicating that tides have played a limited role in their dynamical evolution. On the other hand, TOI-148, the companion with the shortest orbital period in this study, 4.87 days, orbits around an F dwarf, and is circular, thus somewhat strengthening this tendency for close-in massive companions to be found preferentially around F dwarfs (Guillot et al. 2014). A deeper, quantitative study is warranted. The relative lack of these companions around K dwarfs and their presence around M dwarfs as shown in Fig. 12 is unexplained.

We display host star metallicity [Fe/H] in Fig. 13 of transiting brown dwarfs and low-mass stars. Figure 13 shows the most common metallicity for brown dwarf host stars is at [Fe/H] ~ 0, which is consistent with previous findings that brown dwarfs are not preferentially found around metal rich stars like hot Jupiters and are more consistent with metallicity distributions of stars without substellar companions or stars with low-mass planets (e.g., Ma & Ge 2014; Mata Sánchez et al. 2014; Maldonado et al. 2019; Adibekyan 2019). Maldonado & Villaver (2017) found that stars with less massive brown dwarfs tend to have higher

[4] http://www.pas.rochester.edu/~emamajek/EEM_dwarf_UBVIJHK_colors_Teff.txt

metallicities than stars with more massive brown dwarfs, which is consistent with the interpretations of Ma & Ge (2014) and Maldonado et al. (2019) that more massive brown dwarfs tend to form more like low-mass stars. Narang et al. (2018) also found that the metallicity of host stars with brown dwarf companions is lower compared to 1–4 $M_{\rm Jup}$ mass objects but similar to more massive (>4 $M_{\rm Jup}$) planets, suggesting similar formation mechanisms for both. Figure 13 has relatively few companions to make significant statistical claims that these populations have inherently different metallicites, but the distribution is still in agreement with a possible separate population for more massive ($\gtrsim$42.5 $M_{\rm Jup}$) brown dwarfs having a metallicity distribution more similar to low-mass stars (Maldonado & Villaver 2017; Kiefer et al. 2021).

5. Conclusion

We report the discovery and characterization of five transiting companions near the hydrogen-burning mass limit detected by TESS as objects of interest: TOI-148 (UCAC4 260-199322), TOI-587 (HD 74162), TOI-681 (TYC 8911-00495-1), TOI-746 (TYC 9177-00082-1), and TOI-1213 (TYC 8970-00020-1). We combine TESS photometry with ground-based photometry and spectra from the CORALIE, CHIRON, TRES, and FEROS spectrographs to find companion masses between 77 and 98 $M_{\rm Jup}$ and companion radii between 0.81 and 1.66 $R_{\rm Jup}$. We found young ages for TOI-587 (from isochrone stellar modeling) and TOI-681 (from cluster membership) and find their companion radii to be relatively larger compared to companions of similar masses, as expected from theoretical isochrone models. However, TOI-681b has a grazing transit making its companion radius not as well-constrained, and TOI-1213b also has a grazing transit that creates an even less well-constrained companion radius. TOI-148 and TOI-746 have relatively older ages and smaller companion radii. TOI-587 is the hottest main-sequence star ($T_{\rm eff} = 9800 \pm 200$ K) known to host a transiting brown dwarf or low-mass star below 150 $M_{\rm Jup}$. We find evidence of spin-orbit synchronization for TOI-148 and TOI-746, tidal circularization for TOI-148, and possible pseudosynchronization at periastron for TOI-1213. The sample of transiting brown dwarfs and low-mass stars we analyzed is still too small to make significant statistical claims; however, their eccentricity and metallicity distributions are still consistent with previous suggestions of two separate populations for lower and higher mass brown dwarfs. These companions are all near the hydrogen-burning mass limit and add to the statistical sample needed to distinguish the population differences between brown dwarfs and low-mass stars.

Acknowledgements. We thank the Swiss National Science Foundation (SNSF) and the Geneva University for their continuous support to our planet low-mass companion search programs. This work was carried out in the frame of the Swiss National Centre for Competence in Research (NCCR) *PlanetS* supported by the Swiss National Science Foundation (SNSF). This publication makes use of The Data & Analysis Center for Exoplanets (DACE), which is a facility based at the University of Geneva (CH) dedicated to extrasolar planet data visualization, exchange, and analysis. DACE is a platform of NCCR *PlanetS* and is available at https://dace.unige.ch. This paper includes data collected by the TESS mission. Funding for the TESS mission is provided by the NASA Explorer Program. We are grateful to the CHIRON team: Todd Henry, Leonardo Paredes, Hodari James, Azmain Nisak, Rodrigo Hinojosa, Roberto Aviles, and Wei-Chun Jao, for carrying out the CHIRON observations and data reduction. This work has made use of data from the European Space Agency (ESA) mission *Gaia*, processed by the *Gaia* Data Processing and Analysis Consortium (DPAC). Funding for the DPAC has been provided by national institutions, in particular the institutions participating in the *Gaia* Multilateral Agreement. This work makes use of observations from the LCOGT network. LCOGT telescope time was granted by NOIRLab through the Mid-Scale Innovations Program (MSIP). MSIP is funded by NSF. We acknowledge support from the French and Italian Polar Agencies, IPEV and PNRA, and from Université Côte d'Azur under Idex UCA-JEDI (ANR-15-IDEX-01). MEarth is funded by the David and Lucile Packard Fellowship for Science and Engineering, the National Science Foundation under grants AST-0807690, AST-1109468, AST-1004488 (Alan T. Waterman Award) and AST-1616624, and the John Templeton Foundation. This publication was made possible through the support of a grant from the John Templeton Foundation. The opinions expressed in this publication are those of the authors and do not necessarily reflect the views of the John Templeton Foundation. This research received funding from the European Research Council (ERC) under the European Union's Horizon 2020 research and innovation programme (grant agreement n° 803193/BEBOP), and from the Science and Technology Facilities Council (STFC; grant n° ST/S00193X/1). Resources supporting this work were provided by the NASA High-End Computing (HEC) Program through the NASA Advanced Supercomputing (NAS) Division at Ames Research Center for the production of the SPOC data products. We acknowledge the use of public TESS Alert data from pipelines at the TESS Science Office and at the TESS Science Processing Operations Center. SG has been supported by STFC through consolidated grants ST/L000733/1 and ST/P000495/1. KKM acknowledges support from the New York Community Trust Fund for Astrophysical Research. AJ acknowledges support from FONDECYT project 1210718, and from ANID - Millennium Science Initiative - ICN12_009. L.A.d.S. is supported by funding from the European Research Council (ERC) under the European Union's Horizon 2020 research and innovation programme (project FOUR ACES grant agreement No 724427).

References

Adams, F. C., & Laughlin, G. 1997, Rev. Mode. Phys., 69, 337
Adams, F. C., & Laughlin, G. 2006, ApJ, 649, 1004
Adibekyan, V. 2019, Geosciences, 9, 105
Artigau, É., Hébrard, G., Cadieux, C., et al. 2021, AJ, submitted [arXiv:2106.04536]
Asplund, M., Grevesse, N., Sauval, A. J., & Scott, P. 2009, ARA&A, 47, 481
Baraffe, I., Chabrier, G., Allard, F., & Hauschildt, P. H. 2002, A&A, 382, 563
Baraffe, I., Chabrier, G., Barman, T. S., Allard, F., & Hauschildt, P. H. 2003, A&A, 402, 701
Baraffe, I., Homeier, D., Allard, F., & Chabrier, G. 2015, A&A, 577, A42
Barker, A. J., & Ogilvie, G. I. 2009, MNRAS, 395, 2268
Barnes, R. 2017, Celest. Mecha. Dyn. Astron., 129, 509
Bayliss, D., Hojjatpanah, S., Santerne, A., et al. 2017, AJ, 153, 15
Beatty, T. G., Fernández, J. M., Latham, D. W., et al. 2007, ApJ, 663, 573
Benni, P., Burdanov, A. Y., Krushinsky, V. V., et al. 2021, MNRAS, 505, 4956
Blanco-Cuaresma, S., Soubiran, C., Heiter, U., & Jofré, P. 2014, A&A, 569, A111
Bonomo, A. S., Sozzetti, A., Santerne, A., et al. 2015, A&A, 575, A85
Borucki, W. J., Koch, D., Basri, G., et al. 2010, Science, 327, 977
Boss, A. P. 1997, Science, 276, 1836
Bouchy, F., Deleuil, M., Guillot, T., et al. 2011, A&A, 525, A68
Brahm, R., Jordán, A., & Espinoza, N. 2017, PASP, 129, 034002
Brahm, R., Nielsen, L. D., Wittenmyer, R. A., et al. 2020, AJ, 160, 235
Buder, S., Asplund, M., Duong, L., et al. 2018, MNRAS, 478, 4513
Burrows, A., Hubbard, W. B., Lunine, J. I., & Liebert, J. 2001, Rev. Mod. Phys., 73, 719
Cañas, C. I., Bender, C. F., Mahadevan, S., et al. 2018, ApJ, 861, L4
Cameron, A. G. W. 1978, Moon and Planets, 18, 5
Cantat-Gaudin, T., Vallenari, A., Sordo, R., et al. 2018, A&A, 615, A49
Carmichael, T. W., Latham, D. W., & Vand erburg, A. M. 2019, AJ, 158, 38
Carmichael, T. W., Quinn, S. N., Mustill, A. J., et al. 2020, AJ, 160, 53
Carmichael, T. W., Quinn, S. N., Zhou, G., et al. 2021, AJ, 161, 97
Castelli, F., & Kurucz, R. L. 2004, A&A, 419, 725
Chabrier, G., & Baraffe, I. 1997, A&A, 327, 1039
Chabrier, G., Gallardo, J., & Baraffe, I. 2007, A&A, 472, L17
Chatterjee, S., Ford, E. B., Matsumura, S., & Rasio, F. A. 2008, ApJ, 686, 580
Chaturvedi, P., Chakraborty, A., Anandarao, B. G., Roy, A., & Mahadevan, S. 2016, MNRAS, 462, 554
Choi, J., Dotter, A., Conroy, C., et al. 2016, ApJ, 823, 102
Claret, A., & Bloemen, S. 2011, A&A, 529, A75
Collins, K. A., Kielkopf, J. F., Stassun, K. G., & Hessman, F. V. 2017, AJ, 153, 77
Csizmadia, S., Hatzes, A., Gandolfi, D., et al. 2015, A&A, 584, A13
Cummings, J. D., & Kalirai, J. S. 2018, AJ, 156, 165
Dahm, S. E. 2015, ApJ, 813, 108
David, T. J., Hillenbrand, L. A., Gillen, E., et al. 2019, ApJ, 872, 161
Deleuil, M., Deeg, H. J., Alonso, R., et al. 2008, A&A, 491, 889
Díaz, R. F., Damiani, C., Deleuil, M., et al. 2013, A&A, 551, L9
Díaz, R. F., Montagnier, G., Leconte, J., et al. 2014, A&A, 572, A109
Dieterich, S. B., Henry, T. J., Jao, W.-C., et al. 2014, AJ, 147, 94

Dieterich, S. B., Weinberger, A. J., Boss, A. P., et al. 2018, ApJ, 865, 28
Dotter, A. 2016, ApJS, 222, 8
Doyle, A. P., Davies, G. R., Smalley, B., Chaplin, W. J., & Elsworth, Y. 2014, MNRAS, 444, 3592
Dupuy, T. J., & Liu, M. C. 2017, ApJS, 231, 15
Eastman, J. 2017, EXOFASTv2: Generalized publication-quality exoplanet modeling code
Eastman, J., Gaudi, B. S., & Agol, E. 2013, PASP, 125, 83
Eastman, J. D., Rodriguez, J. E., Agol, E., et al. 2019, ArXiv e-prints [arXiv:1907.09480]
Ferraz-Mello, S., Rodríguez, A., & Hussmann, H. 2008, Celest. Mech. Dyn. Astron., 101, 171
Findeisen, K., Hillenbrand, L., & Soderblom, D. 2011, AJ, 142, 23
Fleming, D. P., Barnes, R., Graham, D. E., Luger, R., & Quinn, T. R. 2018, ApJ, 858, 86
Fleming, D. P., Barnes, R., Davenport, J. R. A., & Luger, R. 2019, ApJ, 881, 88
Ford, E. B. 2006, ApJ, 642, 505
Ford, E. B., & Rasio, F. A. 2008, ApJ, 686, 621
Fritzewski, D. J., Barnes, S. A., James, D. J., & Strassmeier, K. G. 2020, A&A, 641, A51
Gaia Collaboration (Brown, A. G. A., et al.) 2018, A&A, 616, A1
Gelman, A., & Rubin, D. B. 1992, Stat. Sci., 7, 457
Gelman, A., Carlin, J. B., Stern, H. S., & Rubin, D. B. 2003, Bayesian Data Analysis, 2nd edn. (London: Chapman & Hall)
Gill, S., Maxted, P. F. L., & Smalley, B. 2018, A&A, 612, A111
Gill, S., Maxted, P. F. L., Evans, J. A., et al. 2019, A&A, 626, A119
Gill, S., Cooke, B. F., Bayliss, D., et al. 2020, MNRAS, 495, 2713
Gillen, E., Hillenbrand, L. A., David, T. J., et al. 2017, ApJ, 849, 11
Goldreich, P., & Soter, S. 1966, Icarus, 5, 375
Gray, R. O., & Corbally, C. J. 1994, AJ, 107, 742
Grether, D., & Lineweaver, C. H. 2006, ApJ, 640, 1051
Grieves, N., Ge, J., Thomas, N., et al. 2017, MNRAS, 467, 4264
Grieves, N., Nielsen, L. D., Vines, J. I., et al. 2021, A&A, 647, A180
Guillot, T., Lin, D. N. C., Morel, P., Havel, M., & Parmentier, V. 2014, EAS Pub. Ser., 65, 327
Gustafsson, B., Edvardsson, B., Eriksson, K., et al. 2008, A&A, 486, 951
Hatzes, A. P., & Rauer, H. 2015, ApJ, 810, L25
Heller, R., Leconte, J., & Barnes, R. 2011, A&A, 528, A27
Hennebelle, P., & Chabrier, G. 2008, ApJ, 684, 395
Hodžić, V., Triaud, A. H. M. J., Anderson, D. R., et al. 2018, MNRAS, 481, 5091
Howell, S. B., Sobeck, C., Haas, M., et al. 2014, PASP, 126, 398
Huang, C. X., Vanderburg, A., Pál, A., et al. 2020a, Res. Notes Am. Astron. Soc., 4, 204
Huang, C. X., Vanderburg, A., Pál, A., et al. 2020b, Res. Notes Am. Astron. Soc., 4, 206
Husser, T. O., Wende-von Berg, S., Dreizler, S., et al. 2013, A&A, 553, A6
Hut, P. 1981, A&A, 99, 126
Irwin, J., Buchhave, L., Berta, Z. K., et al. 2010, ApJ, 718, 1353
Irwin, J. M., Charbonneau, D., Esquerdo, G. A., et al. 2018, AJ, 156, 140
Jackman, J. A. G., Wheatley, P. J., Bayliss, D., et al. 2019, MNRAS, 489, 5146
Jeffries, R. D., Thurston, M. R., & Pye, J. P. 1997, MNRAS, 287, 350
Jeffries, R. D., James, D. J., & Thurston, M. R. 1998, MNRAS, 300, 550
Jenkins, J. M. 2002, ApJ, 575, 493
Jenkins, J. M., Chandrasekaran, H., McCauliff, S. D., et al. 2010, SPIE Conf. Ser., 7740, 77400D
Jenkins, J. M., Twicken, J. D., McCauliff, S., et al. 2016, SPIE Conf. Ser., 9913, 99133E
Jensen, E. 2013, Astrophysics Source Code Library [record ascl:1306.007]
Johnson, J. A., Apps, K., Gazak, J. Z., et al. 2011, ApJ, 730, 79
Jordán, A., Brahm, R., Espinoza, N., et al. 2020, AJ, 159, 145
Kaufer, A., Stahl, O., Tubbesing, S., et al. 1999, The Messenger, 95, 8
Kiefer, F., Hébrard, G., Sahlmann, J., et al. 2019, A&A, 631, A125
Kiefer, F., Hébrard, G., Lecavelier des Etangs, A., et al. 2021, A&A, 645, A7
Kounkel, M., & Covey, K. 2019, AJ, 158, 122
Li, J., Tenenbaum, P., Twicken, J. D., et al. 2019, PASP, 131, 024506
Lorenzo-Oliveira, D., Meléndez, J., Yana Galarza, J., et al. 2019, MNRAS, 485, L68
Lucy, L. B., & Sweeney, M. A. 1971, AJ, 76, 544
Ma, B., & Ge, J. 2014, MNRAS, 439, 2781
Maldonado, J., & Villaver, E. 2017, A&A, 602, A38
Maldonado, J., Villaver, E., Eiroa, C., & Micela, G. 2019, A&A, 624, A94
Mamajek, E. E., & Hillenbrand, L. A. 2008, ApJ, 687, 1264
Marcy, G. W., & Butler, R. P. 2000, PASP, 112, 137
Mata Sánchez, D., González Hernández, J. I., Israelian, G., et al. 2014, A&A, 566, A83
Mazeh, T. 2008, EAS Pub. Ser., 29, 1
Meingast, S., Alves, J., & Rottensteiner, A. 2021, A&A, 645, A84
Mireles, I., Shporer, A., Grieves, N., et al. 2020, AJ, 160, 133
Moutou, C., Bonomo, A. S., Bruno, G., et al. 2013, A&A, 558, L6
Narang, M., Manoj, P., Furlan, E., et al. 2018, AJ, 156, 221
Nefs, S. V., Birkby, J. L., Snellen, I. A. G., et al. 2013, MNRAS, 431, 3240
Nowak, G., Palle, E., Gandolfi, D., et al. 2017, AJ, 153, 131
Ofir, A., Gandolfi, D., Buchhave, L., et al. 2012, MNRAS, 423, L1
Padoan, P., & Nordlund, Å. 2004, ApJ, 617, 559
Palle, E., Luque, R., Zapatero Osorio, M. R., et al. 2021, A&A, 650, A55
Paredes. 2021, AJ, submitted
Parsons, S. G., Gänsicke, B. T., Marsh, T. R., et al. 2012a, MNRAS, 426, 1950
Parsons, S. G., Marsh, T. R., Gänsicke, B. T., et al. 2012b, MNRAS, 419, 304
Parsons, S. G., Marsh, T. R., Gänsicke, B. T., et al. 2012c, MNRAS, 420, 3281
Paxton, B., Marchant, P., Schwab, J., et al. 2015, ApJS, 220, 15
Pecaut, M. J., & Mamajek, E. E. 2013, ApJS, 208, 9
Pepe, F., Mayor, M., Rupprecht, G., et al. 2002, The Messenger, 110, 9
Persson, C. M., Csizmadia, S., Mustill, A. e. J., et al. 2019, A&A, 628, A64
Piskunov, N. E., & Valenti, J. A. 2002, A&A, 385, 1095
Pollack, J. B., Hubickyj, O., Bodenheimer, P., et al. 1996, Icarus, 124, 62
Pont, F., Bouchy, F., Melo, C., et al. 2005a, A&A, 438, 1123
Pont, F., Melo, C. H. F., Bouchy, F., et al. 2005b, A&A, 433, L21
Pont, F., Moutou, C., Bouchy, F., et al. 2006, A&A, 447, 1035
Queloz, D., Mayor, M., Udry, S., et al. 2001, The Messenger, 105, 1
Randich, S., Tognelli, E., Jackson, R., et al. 2018, A&A, 612, A99
Rasio, F. A., & Ford, E. B. 1996, Science, 274, 954
Ricker, G. R., Winn, J. N., Vanderspek, R., et al. 2015, J. Astron. Teles. Instrum. Syst., 1, 014003
Robles, J. A., Lineweaver, C. H., Grether, D., et al. 2008, ApJ, 684, 691
Sadeghi Ardestani, L., Guillot, T., & Morel, P. 2017, MNRAS, 472, 2590
Sahlmann, J., Ségransan, D., Queloz, D., et al. 2011, A&A, 525, A95
Santerne, A., Moutou, C., Tsantaki, M., et al. 2016, A&A, 587, A64
Schlecker, M., Kossakowski, D., Brahm, R., et al. 2020, AJ, 160, 275
Schlegel, D. J., Finkbeiner, D. P., & Davis, M. 1998, ApJ, 500, 525
Shporer, A., Zhou, G., Vanderburg, A., et al. 2017, ApJ, 847, L18
Siverd, R. J., Beatty, T. G., Pepper, J., et al. 2012, ApJ, 761, 123
Skumanich, A. 1972, ApJ, 171, 565
Smith, J. C., Stumpe, M. C., Van Cleve, J. E., et al. 2012, PASP, 124, 1000
Soderblom, D. R., Hillenbrand, L. A., Jeffries, R. D., Mamajek, E. E., & Naylor, T. 2014, Protostars and Planets VI (Tucson: University of Arizona Press), 219
Spiegel, D. S., Burrows, A., & Milsom, J. A. 2011, ApJ, 727, 57
Stassun, K. G., & Torres, G. 2016, AJ, 152, 180
Stassun, K. G., & Torres, G. 2018, ApJ, 862, 61
Stassun, K. G., Mathieu, R. D., & Valenti, J. A. 2006, Nature, 440, 311
Stassun, K. G., Collins, K. A., & Gaudi, B. S. 2017, AJ, 153, 136
Stassun, K. G., Corsaro, E., Pepper, J. A., & Gaudi, B. S. 2018, AJ, 155, 22
Stumpe, M. C., Smith, J. C., Van Cleve, J. E., et al. 2012, PASP, 124, 985
Stumpe, M. C., Smith, J. C., Catanzarite, J. H., et al. 2014, PASP, 126, 100
Šubjak, J., Sharma, R., Carmichael, T. W., et al. 2020, AJ, 159, 151
Tal-Or, L., Mazeh, T., Alonso, R., et al. 2013, A&A, 553, A30
Thompson, G. I., Nandy, K., Jamar, C., et al. 1978, Catalogue of stellar ultraviolet fluxes: a compilation of absolute stellar fluxes measured by the Sky Survey Telescope (S2/68) aboard the ESRO satellite TD-1 /
Tokovinin, A. 2018, PASP, 130, 035002
Tokovinin, A., Fischer, D. A., Bonati, M., et al. 2013, PASP, 125, 1336
Torres, G., Andersen, J., & Giménez, A. 2010, A&ARv, 18, 67
Triaud, A. H. M. J., Hebb, L., Anderson, D. R., et al. 2013, A&A, 549, A18
Triaud, A. H. M. J., Burgasser, A. J., Burdanov, A., et al. 2020, Nat. Astron., 4, 650
Twicken, J. D., Catanzarite, J. H., Clarke, B. D., et al. 2018, PASP, 130, 064502
Verbunt, F., & Zwaan, C. 1981, A&A, 100, L7
von Boetticher, A., Triaud, A. H. M. J., Queloz, D., et al. 2019, A&A, 625, A150
Whitworth, A. 2018, ArXiv e-prints [arXiv:1811.06833]
Winn, J. N., Noyes, R. W., Holman, M. J., et al. 2005, ApJ, 631, 1215
Witte, M. G., & Savonije, G. J. 2002, A&A, 386, 222
Yee, S. W., Petigura, E. A., & von Braun K. 2017, ApJ, 836, 77
Zahn, J. P. 1977, A&A, 500, 121
Zahn, J. P., & Bouchet, L. 1989, A&A, 223, 112
Zhou, G., Bayliss, D., Hartman, J. D., et al. 2014, MNRAS, 437, 2831
Zhou, G., Bakos, G. Á., Bayliss, D., et al. 2019, AJ, 157, 31
Zhou, G., Winn, J. N., Newton, E. R., et al. 2020, ApJ, 892, L21
Ziegler, C., Tokovinin, A., Briceno, C., et al. 2020, VizieR Online Data Catalog: J/AJ/159/19
Zimmerman, M. K., Thompson, S. E., Mullally, F., et al. 2017, ApJ, 846, 147

[1] Observatoire de Genève, Université de Genève, 51 Ch. des Maillettes, 1290 Sauverny, Switzerland
e-mail: nolan.grieves@unige.ch
[2] Harvard University, Cambridge, MA 02138, USA

[3] Center for Astrophysics, Harvard & Smithsonian, 60 Garden Street, Cambridge, MA 02138, USA
[4] Department of Physics and Astronomy, University of New Mexico, 210 Yale Blvd NE, Albuquerque, NM 87106, USA
[5] Department of Physics and Kavli Institute for Astrophysics and Space Research, Massachusetts Institute of Technology, Cambridge, MA 02139, USA
[6] Department of Astronomy, Wellesley College, Wellesley, MA 02481, USA
[7] Facultad de Ingeniería y Ciencias, Universidad Adolfo Ibáñez, Av. Diagonal las Torres 2640, Peñalolén, Santiago, Chile
[8] Millennium Institute for Astrophysics, Chile
[9] Vanderbilt University, Department of Physics & Astronomy, 6301 Stevenson Center Lane, Nashville, TN 37235, USA
[10] Department of Physics, University of Warwick, Gibbet Hill Road, Coventry, CV4 7AL, UK
[11] Centre for Exoplanets and Habitability, University of Warwick, Gibbet Hill Road, Coventry, CV4 7AL, UK
[12] Department of Astrophysical Sciences, Princeton University, 4 Ivy Lane, Princeton, NJ 08540, USA
[13] Université Côte d'Azur, Observatoire de la Côte d'Azur, CNRS, Laboratoire Lagrange, Bd de l'Observatoire, CS 34229, 06304 Nice cedex 4, France
[14] University of Grenoble Alpes, CNRS, IPAG, 38000 Grenoble, France
[15] School of Physics and Astronomy, University of Leicester, LE1 7RH, UK
[16] NASA Ames Research Center, Moffett Field, CA 94035, USA
[17] Max-Planck-Institut für Astronomie, Königstuhl 17, 69117 Heidelberg, Germany
[18] Institute for Advanced Study, Princeton, NJ 08540, USA
[19] George Mason University, 4400 University Drive, Fairfax, VA, 22030 USA
[20] NASA Goddard Space Flight Center, Exoplanets and Stellar Astrophysics Laboratory (Code 667), Greenbelt, MD 20771, USA
[21] European Space Agency (ESA), European Space Research and Technology Centre (ESTEC), Keplerlaan 1, 2201 AZ Noordwijk, The Netherlands
[22] School of Physics & Astronomy, University of Birmingham, Edgbaston, Birmingham B15 2TT, UK
[23] El Sauce Observatory, Coquimbo Province, Chile
[24] Centre for Astrophysics, University of Southern Queensland, Toowoomba, QLD, 4350, Australia
[25] Dept. of Physics & Astronomy, Swarthmore College, Swarthmore PA 19081, USA
[26] Department of Physics and Astronomy, University of Louisville, Louisville, KY 40292, USA
[27] Concordia Station, IPEV/PNRA, Antarctica
[28] Ellinbank Observatory, Australia
[29] Brierfield Observatory, New South Wales, Australia
[30] Space Telescope Science Institute, 3700 San Martin Drive, Baltimore, MD, 21218, USA
[31] Royal Astronomical Society, Burlington House, Piccadilly, London W1J 0BQ, UK
[32] Patashnick Voorheesville Observatory, Voorheesville, NY 12186, USA
[33] SETI Institute, Mountain View, CA 94043, USA
[34] Hazelwood Observatory, Australia
[35] Perth Exoplanet Survey Telescope, Perth, Western Australia
[36] Department of Astrophysical and Planetary Sciences, University of Colorado, Boulder, CO 80309, USA
[37] Mt. Stuart Observatory, New Zealand

Appendix A: Supplementary material

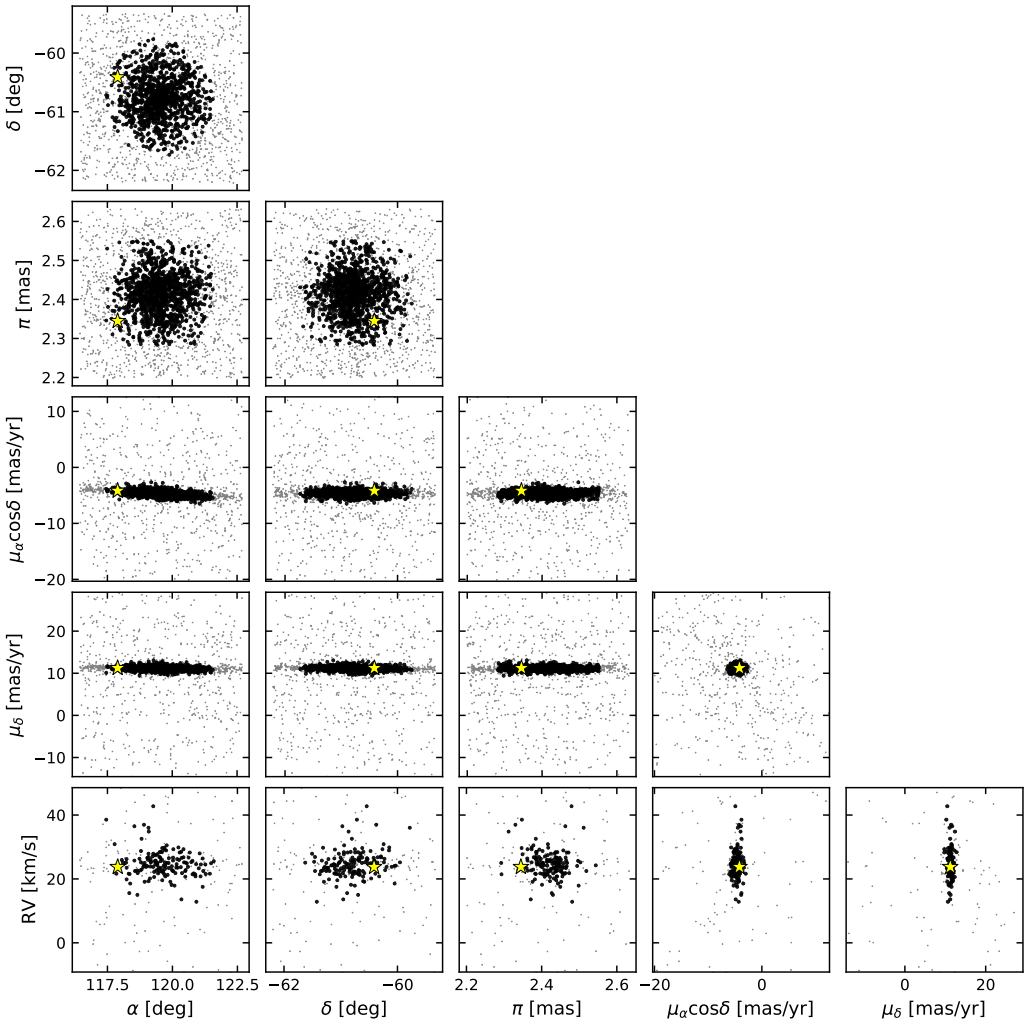

Fig. A.1. Kinematic analysis of TOI-681 exhibiting its membership to the open star cluster NGC 2516. Black points are NGC 2516 members reported by Cantat-Gaudin et al. (2018). Gray points are randomly drawn from a cube in $\{\alpha, \delta, \pi\}$ centered on the cluster, with side widths $\pm 4\sigma$, where σ is the standard deviation of the Cantat-Gaudin et al. (2018) cluster member right ascension, declination, and parallax.

Table A.1. Radial Velocities.

Time [BJD TDB]	RV [m s^{-1}]	RV error [m s^{-1}]	Instrument
TOI-148			
2 458 384.515064	–30 660.46	30.42	CORALIE
2 458 386.814005	–37 976.20	82.56	CORALIE
2 458 408.719335	–20 372.36	85.21	CORALIE
2 458 428.534714	–20 473.55	63.01	CORALIE
2 458 479.532552	–38 130.30	191.13	CORALIE
2 458 495.531823	–25 865.29	221.07	CORALIE
2 458 496.547259	–20 001.33	122.21	CORALIE
2 458 656.803753	–20 849.44	130.90	CORALIE
2 458 657.770975	–23 724.86	115.92	CORALIE
2 458 663.857660	–35 835.81	149.59	CORALIE
2 458 679.761215	–33 895.58	178.17	CORALIE
TOI-587			
2 458 589.719888	376.98	1201.42	TRES
2 458 594.622423	–8024.60	637.52	TRES
2 458 597.701320	3.14	821.62	TRES
2 458 598.631813	1292.14	745.23	TRES
2 458 599.640043	0.00	821.62	TRES
2 458 601.636267	–6391.02	604.17	TRES
2 458 603.630556	–6396.90	1140.20	TRES
TOI-681			
2 458 622.513448	26 180.44	88.22	CORALIE
2 458 654.485737	26 094.93	78.95	CORALIE
2 458 818.766341	16 662.76	114.76	CORALIE
2 458 819.812002	17 277.56	102.12	CORALIE
2 458 842.699941	27 731.61	128.99	CORALIE
2 458 850.641613	17 162.30	84.73	CORALIE
2 458 852.779240	18 827.26	102.06	CORALIE
2 458 857.727110	27 269.20	85.20	CORALIE
2 458 923.549796	24 577.10	130.60	CORALIE
2 458 641.493741	23 125.7	349.9	FEROS
2 458 643.486061	20 111.0	213.9	FEROS
2 458 645.490361	18 394.8	331.0	FEROS
2 458 652.498401	29 384.2	605.8	FEROS
TOI-746			
2 458 777.827622	26 662.93	63.11	CORALIE
2 458 815.804367	39 986.84	44.16	CORALIE
2 458 820.773420	25 318.60	40.97	CORALIE
2 458 824.651474	35 494.88	63.08	CORALIE
2 458 830.772597	27 610.22	45.59	CORALIE
2 458 839.622606	38 959.05	71.50	CORALIE
2 458 844.682083	29 562.96	70.22	CORALIE
2 458 920.561788	26 623.69	100.59	CORALIE
2 458 798.773421	25 294.4	10.3	FEROS
2 458 804.702041	39 780.9	7.9	FEROS
TOI-1213			
2 458 886.78385	19 685.0	30.0	CHIRON
2 458 909.72687	21 761.0	29.0	CHIRON
2 458 917.78559	19 130.0	30.0	CHIRON
2 458 883.615306	22 638.52	24.61	CORALIE
2 458 895.675990	34 772.99	70.44	CORALIE
2 458 920.746399	27 968.23	57.41	CORALIE
2 458 925.564278	31 941.32	69.56	CORALIE
2 458 882.839021	23 064.1	6.0	FEROS
2 458 908.787371	23 728.5	7.6	FEROS
2 458 915.735351	20 533.3	7.2	FEROS

Table A.2. TOI-148 stellar and companion parameters.

Star name & aliases: TOI 148, TIC 393 940 766, UCAC4 260-199 322, 2MASS J22331696-3 809 349			
Parameter	Unit	Source	Value
Stellar parameters			
α	Right ascension (hh:mm:ss)	TICv8	22:33:16.99
δ	Declination (deg:min:sec)	TICv8	–38:09:35.38
$V_{\rm mag}$	V-band magnitude	TICv8	12.40
ϖ	Parallax (mas)	*Gaia* DR2	2.441 ± 0.017
$v \sin i_*$	Surface rotational velocity (km s^{-1})	CORALIE	10.1 ± 0.8
Parameter	Unit	Exofast priors	Value
M_*	Mass ($M_\odot$)	–	$0.97^{+0.12}_{-0.09}$
R_*	Radius ($R_\odot$)	$\mathcal{G}$[1.192,0.068]	$1.20^{+0.07}_{-0.07}$
L_*	Luminosity ($L_\odot$)	–	$1.66^{+0.26}_{-0.23}$
ρ_*	Density (cgs)	–	$0.80^{+0.17}_{-0.12}$
$\log g$	Surface gravity (cgs)	–	$4.27^{+0.06}_{-0.06}$
$T_{\rm eff}$	Effective temperature (K)	$\mathcal{G}$[5975,150]	5990^{+140}_{-140}
[Fe/H]	Metallicity (dex)	$\mathcal{G}$[-0.28,0.28]	$-0.24^{+0.25}_{-0.25}$
Age	Age (Gyr)	–	$7.7^{+3.7}_{-3.7}$
EEP	Equal evolutionary point	–	416^{+17}_{-41}
Companion parameters			
M_b	Mass ($M_{\rm J}$)	–	$77.1^{+5.8}_{-4.6}$
R_b	Radius ($R_{\rm J}$)	–	$0.81^{+0.05}_{-0.06}$
P	Period (days)	–	$4.867103^{+0.000015}_{-0.000014}$
T_C	Time of conjunction (BJD$_{\rm TDB}$)	–	$2458327.32980^{+0.00200}_{-0.00210}$
a	Semi-major axis (AU)	–	$0.0571^{+0.0021}_{-0.0017}$
i	Inclination (Degrees)	–	$86.85^{+0.65}_{-0.53}$
e	Eccentricity	–	$0.0052^{+0.0060}_{-0.0037}$
ω_*	Argument of Periastron (Degrees)	–	$-63.0^{+87.0}_{-71.0}$
$T_{\rm eq}$	Equilibrium temperature (K)	–	1321^{+46}_{-49}
K	RV semi-amplitude (m s^{-1})	–	$8950.0^{+51.0}_{-52.0}$
δ	Transit depth (fraction)	–	$0.00476^{+0.00017}_{-0.00017}$
τ	Ingress/egress transit duration (days)	–	$0.01280^{+0.00170}_{-0.00170}$
T_{14}	Total transit duration (days)	–	$0.13790^{+0.00200}_{-0.00200}$
b	Transit impact parameter	–	$0.565^{+0.061}_{-0.088}$
ρ_P	Density (cgs)	–	$183.0^{+45.0}_{-32.0}$
$\log g_{\rm P}$	Surface gravity	–	$5.471^{+0.066}_{-0.059}$
$\langle F \rangle$	Incident flux (10^9 erg s^{-1} cm^{-2})	–	$0.69^{+0.10}_{-0.10}$

Wavelength parameters		R	Sloani	TESS
u_1	linear limb-darkening coeff	$0.314^{+0.056}_{-0.055}$	$0.259^{+0.033}_{-0.031}$	$0.262^{+0.041}_{-0.040}$
u_2	quadratic limb-darkening coeff	$0.304^{+0.051}_{-0.051}$	$0.291^{+0.026}_{-0.026}$	$0.294^{+0.035}_{-0.035}$

RV Parameters		CORALIE
$\gamma_{\rm rel}$	Relative RV Offset (m s^{-1})	$-29\,137^{+52}_{-53}$
σ_J	RV Jitter (m s^{-1})	69^{+23}_{-54}
σ_J^2	RV Jitter variance	4800^{+3600}_{-4500}

Notes. Priors are for the EXOFASTv2 global model only, where $\mathcal{G}$[a,b] are Gaussian priors. The topmost parameters were not modeled with EXOFASTv2 and the source of their value is displayed.

Table A.3. TOI-587 stellar and companion parameters.

Star name & aliases: TOI 587, TIC 294 090 620, HD 74162, HIP 42654, TYC 6024-00943-1, 2MASS J08413504-2 211 395			
Parameter	Unit	Source	Value
Stellar parameters			
α	Right ascension (hh:mm:ss)	TICv8	08:41:35.02
δ	Declination (deg:min:sec)	TICv8	–22:11:39.47
$V_{\rm mag}$	V-band magnitude	TICv8	7.8
ϖ	Parallax (mas)	*Gaia* DR2	4.755±0.028
$v \sin i_*$	Surface rotational velocity (km s^{-1})	TRES	34.0±2.0
Parameter	Unit	Exofast Priors	Value
M_*	Mass ($M_\odot$)	–	$2.33^{+0.12}_{-0.12}$
R_*	Radius ($R_\odot$)	$\mathcal{G}$[2.031,0.092]	$2.01^{+0.09}_{-0.09}$
L_*	Luminosity ($L_\odot$)	–	$33.50^{+4.20}_{-3.90}$
ρ_*	Density (cgs)	–	$0.41^{+0.06}_{-0.05}$
$\log g$	Surface gravity (cgs)	–	$4.20^{+0.04}_{-0.04}$
$T_{\rm eff}$	Effective Temperature (K)	$\mathcal{G}$[9800,200]	9800^{+200}_{-200}
[Fe/H]	Metallicity (dex)	$\mathcal{G}$[0.07,0.12]	$0.08^{+0.11}_{-0.12}$
Age	Age (Gyr)	–	$0.2^{+0.1}_{-0.1}$
EEP	Equal evolutionary point	–	326^{+11}_{-16}
Companion parameters			
M_b	Mass ($M_{\rm J}$)	–	$81.1^{+7.1}_{-7.0}$
R_b	Radius ($R_{\rm J}$)	–	$1.32^{+0.07}_{-0.06}$
P	Period (days)	–	$8.043450^{+0.000730}_{-0.000720}$
T_C	Time of conjunction (BJD$_{\rm TDB}$)	–	$2458520.15829^{+0.00053}_{-0.00053}$
a	Semi-major axis (AU)	–	$0.1054^{+0.0018}_{-0.0018}$
i	Inclination (Degrees)	–	$87.93^{+1.00}_{-0.63}$
e	Eccentricity	–	$0.0510^{+0.0490}_{-0.0360}$
ω_*	Argument of Periastron (Degrees)	–	$70.0^{+100.0}_{-100.0}$
T_{eq}	Equilibrium temperature (K)	–	2062^{+55}_{-56}
K	RV semi-amplitude (m s^{-1})	–	$4580.0^{+360.0}_{-360.0}$
δ	Transit depth (fraction)	–	$0.00459^{+0.00008}_{-0.00008}$
τ	Ingress/egress transit duration (days)	–	$0.01660^{+0.00260}_{-0.00220}$
T_{14}	Total transit duration (days)	–	$0.22080^{+0.00240}_{-0.00200}$
b	Transit impact parameter	–	$0.400^{+0.120}_{-0.200}$
ρ_P	Density (cgs)	–	$43.3^{+7.6}_{-6.5}$
log g$_P$	Surface gravity	–	$5.059^{+0.053}_{-0.054}$
$\langle F \rangle$	Incident flux (10^9 erg s^{-1} cm^{-2})	–	$4.09^{+0.46}_{-0.42}$

Wavelength parameters		TESS
u_1	linear limb-darkening coeff	$0.133^{+0.057}_{-0.058}$
u_2	quadratic limb-darkening coeff	$0.245^{+0.085}_{-0.086}$

RV Parameters		TRES
$\gamma_{\rm rel}$	Relative RV Offset (m s^{-1})	-3280^{+330}_{-320}
σ_J	RV Jitter (m s^{-1})	0^{+82}_{-0}
σ_J^2	RV Jitter Variance	-100^{+6900}_{-6700}

Notes. Priors are for the EXOFASTv2 global model only, where $\mathcal{G}$[a,b] are Gaussian priors. The topmost parameters were not modeled with EXOFASTv2 and the source of their value is displayed.

Table A.4. TOI-681 stellar and companion parameters.

Star name & aliases: TOI 681, TIC 410 450 228, TYC 8911-00495-1, UCAC4 148-012283, 2MASS J07513479-6 024 448			
Parameter	Unit	Source	Value
Stellar parameters			
α	Right Ascension (hh:mm:ss)	TICv8	07:51:34.79
δ	Declination (deg:min:sec)	TICv8	–60:24:44.6
$V_{\rm mag}$	V-band magnitude	TICv8	10.885
ϖ	Parallax (mas)	*Gaia* DR2	2.442±0.013
$v \sin i_*$	Surface rotational velocity (km s^{-1})	GALAH	30.80 ± 0.78
Parameter	Unit	Exofast Priors	Value
M_*	Mass ($M_\odot$)	–	$1.54^{+0.06}_{-0.05}$
R_*	Radius ($R_\odot$)	$\mathcal{G}$[1.586,0.067]	$1.47^{+0.04}_{-0.04}$
L_*	Luminosity ($L_\odot$)	–	$5.98^{+0.65}_{-0.58}$
ρ_*	Density (cgs)	–	$0.68^{+0.05}_{-0.05}$
$\log g$	Surface gravity (cgs)	–	$4.29^{+0.02}_{-0.02}$
$T_{\rm eff}$	Effective temperature (K)	$\mathcal{G}$[7390,150]	7440^{+150}_{-140}
[Fe/H]	Metallicity (dex)	$\mathcal{G}$[-0.12,0.05]	$-0.08^{+0.05}_{-0.05}$
Age	Age (Gyr)	$\mathcal{G}$[0.170,0.025]	$0.170^{+0.025}_{-0.025}$ (†)
EEP	Equal evolutionary point	–	264^{+6}_{-7}
Companion parameters			
M_b	Mass ($M_{\rm J}$)	–	$88.7^{+2.5}_{-2.3}$
R_b	Radius ($R_{\rm J}$)	[0,5]	$1.52^{+0.25}_{-0.15}$
P	Period (days)	–	$15.778482^{+0.000026}_{-0.000026}$
T_C	Time of conjunction - 2 450 000 (BJD$_{\rm TDB}$)	–	$2458546.47759^{+0.00068}_{-0.00069}$
a	Semi-major axis (AU)	–	$0.1449^{+0.0018}_{-0.0017}$
i	Inclination (Degrees)	–	$87.62^{+0.09}_{-0.11}$
e	Eccentricity	–	$0.0930^{+0.0220}_{-0.0190}$
ω_*	Argument of Periastron (Degrees)	–	$-86.5^{+7.2}_{-5.6}$
T_{eq}	Equilibrium temperature (K)	–	1143^{+26}_{-25}
K	RV semi-amplitude (m s^{-1})	–	$5209.0^{+72.0}_{-67.0}$
δ	Transit depth (fraction)	–	$0.01120^{+0.00340}_{-0.00170}$
τ	Ingress/egress transit duration (days)	–	$0.07207^{+0.00085}_{-0.00084}$
T_{14}	Total transit duration (days)	–	$0.14410^{+0.00170}_{-0.00170}$
b	Transit impact parameter	–	$0.958^{+0.025}_{-0.017}$
ρ_P	Density (cgs)	–	$31.0^{+11.0}_{-11.0}$
log g$_P$	Surface gravity	–	$4.979^{+0.086}_{-0.130}$
$\langle F \rangle$	Incident Flux (10^9 erg s^{-1} cm^{-2})	–	$0.38^{+0.04}_{-0.03}$

Wavelength parameters		B	I	R	Sloang	TESS
u_1	linear limb-darkening coeff	$0.362^{+0.048}_{-0.048}$	$0.180^{+0.034}_{-0.034}$	$0.132^{+0.046}_{-0.046}$	$0.376^{+0.045}_{-0.045}$	$0.153^{+0.033}_{-0.033}$
u_2	quadratic limb-darkening coeff	$0.336^{+0.049}_{-0.049}$	$0.350^{+0.034}_{-0.035}$	$0.278^{+0.047}_{-0.048}$	$0.370^{+0.046}_{-0.047}$	$0.320^{+0.033}_{-0.034}$

RV parameters		CORALIE	FEROS
$\gamma_{\rm rel}$	Relative RV Offset (m s^{-1})	22120^{+96}_{-87}	23750^{+140}_{-140}
σ_J	RV Jitter (m s^{-1})	95^{+3}_{-7}	0^{+0}_{-0}
σ_J^2	RV Jitter Variance	9040^{+710}_{-1400}	$-23\,000^{+21000}_{-16\,000}$

Notes. Priors are for the EXOFASTv2 global model only, where $\mathcal{G}$[a,b] are Gaussian priors and priors in brackets represent hard limit priors. The topmost parameters were not modeled with EXOFASTv2 and the source of their value is displayed. (†)Age of cluster NGC 2516.

Table A.5. TOI-746 stellar and companion parameters.

Star name & aliases: TOI 746, TIC 167 418 903, TYC 9177-00082-1, UCAC4 112-012172, 2MASS J06382899-6 738 563			
Parameter	Unit	Source	Value
Stellar parameters			
α	Right ascension (hh:mm:ss)	TICv8	06:38:28.99
δ	Declination (deg:min:sec)	TICv8	–67:38:56.22
$V_{\rm mag}$	V-band magnitude	TICv8	11.807
ϖ	Parallax (mas)	*Gaia* DR2	4.167±0.014
$v \sin i_*$	Surface rotational velocity (km s^{-1})	CORALIE	6.1±1.2
Parameter	Unit	Exofast Priors	Value
M_*	Mass ($M_\odot$)	–	$0.94^{+0.09}_{-0.08}$
R_*	Radius ($R_\odot$)	$\mathcal{G}$[0.957,0.051]	$0.97^{+0.04}_{-0.03}$
L_*	Luminosity ($L_\odot$)	–	$0.89^{+0.12}_{-0.11}$
ρ_*	Density (cgs)	–	$1.45^{+0.12}_{-0.13}$
$\log g$	Surface gravity (cgs)	–	$4.44^{+0.03}_{-0.03}$
$T_{\rm eff}$	Effective Temperature (K)	$\mathcal{G}$[5700,150]	5690^{+140}_{-140}
[Fe/H]	Metallicity (dex)	$\mathcal{G}$[0.01,0.29]	$-0.02^{+0.23}_{-0.23}$
Age	Age (Gyr)	–	$6.5^{+4.3}_{-3.9}$
EEP	Equal evolutionary point	–	368^{+30}_{-32}
Companion parameters			
M_b	Mass ($M_{\rm J}$)	–	$82.2^{+4.9}_{-4.4}$
R_b	Radius ($R_{\rm J}$)	–	$0.95^{+0.09}_{-0.06}$
P	Period (days)	–	$10.980303^{+0.000011}_{-0.000011}$
T_C	Time of conjunction - 2 450 000 (BJD$_{\rm TDB}$)	–	$2458335.77067^{+0.00054}_{-0.00054}$
a	Semi-major axis (AU)	–	$0.0973^{+0.0028}_{-0.0026}$
i	Inclination (Degrees)	–	$87.03^{+0.11}_{-0.14}$
e	Eccentricity	–	$0.1985^{+0.0029}_{-0.0031}$
ω_*	Argument of Periastron (Degrees)	–	$116.5^{+1.0}_{-1.0}$
$T_{\rm eq}$	Equilibrium temperature (K)	–	867^{+26}_{-25}
K	RV semi-amplitude (m s^{-1})	–	$7565.0^{+21.0}_{-22.0}$
δ	Transit depth (fraction)	–	$0.01014^{+0.00140}_{-0.00091}$
τ	Ingress/egress transit duration (days)	–	$0.04163^{+0.00071}_{-0.00380}$
T_{14}	Total transit duration (days)	–	$0.08340^{+0.00130}_{-0.00130}$
b	Transit Impact parameter	–	$0.911^{+0.014}_{-0.010}$
ρ_P	Density (cgs)	–	$119.0^{+24.0}_{-27.0}$
log g$_P$	Surface gravity	–	$5.355^{+0.052}_{-0.075}$
$\langle F \rangle$	Incident flux (10^9 erg s^{-1} cm^{-2})	–	$0.12^{+0.01}_{-0.01}$

Wavelength parameters		Sloan u	Sloan z	TESS	V
u_1	linear limb-darkening coeff	$0.830^{+0.088}_{-0.095}$	$0.254^{+0.042}_{-0.042}$	$0.312^{+0.045}_{-0.045}$	$0.469^{+0.067}_{-0.065}$
u_2	quadratic limb-darkening coeff	$0.023^{+0.091}_{-0.088}$	$0.267^{+0.036}_{-0.036}$	$0.271^{+0.037}_{-0.038}$	$0.248^{+0.056}_{-0.057}$

RV parameters		CORALIE	FEROS
$\gamma_{\rm rel}$	Relative RV Offset (m s^{-1})	33547^{+20}_{-22}	33509^{+44}_{-43}
σ_J	RV Jitter (m s^{-1})	0^{+54}_{-0}	62^{+26}_{-32}
σ_J^2	RV Jitter Variance	-400^{+3300}_{-1000}	3900^{+3900}_{-2900}

Notes. Priors are for the EXOFASTv2 global model only, where $\mathcal{G}$[a,b] are Gaussian priors. The topmost parameters were not modeled with EXOFASTv2 and the source of their value is displayed.

Table A.6. TOI-1213 stellar and companion parameters.

Star name & aliases: TOI 1213, TIC 399 144 800, TYC 8970-00020-1, UCAC4 114-034370, 2MASS J10524799-6 723 161			
Parameter	Unit	Source	Value
Stellar parameters			
α	Right ascension (hh:mm:ss)	TICv8	10:52:47.72
δ	Declination (deg:min:sec)	TICv8	–67:23:14.9
$V_{\rm mag}$	V-band magnitude	TICv8	11.54
ϖ	Parallax (mas)	*Gaia* DR2	6.197±0.014
$v \sin i_*$	Surface rotational velocity (km s^{-1})	CORALIE	4.0±1.2
Parameter	Unit	Exofast priors	Value
M_*	Mass ($M_\odot$)	–	$0.99^{+0.07}_{-0.06}$
R_*	Radius ($R_\odot$)	$\mathcal{G}$[0.951,0.059]	$0.99^{+0.04}_{-0.04}$
L_*	Luminosity ($L_\odot$)	–	$0.86^{+0.14}_{-0.12}$
ρ_*	Density (cgs)	–	$1.43^{+0.20}_{-0.13}$
$\log g$	Surface gravity (cgs)	–	$4.44^{+0.04}_{-0.03}$
$T_{\rm eff}$	Effective temperature (K)	$\mathcal{G}$[5675,175]	5590^{+150}_{-150}
[Fe/H]	Metallicity (dex)	$\mathcal{G}$[0.28,0.16]	$0.25^{+0.13}_{-0.14}$
Age	Age (Gyr)	–	$5.3^{+4.2}_{-3.4}$
EEP	Equal evolutionary point	–	355^{+38}_{-30}
Companion parameters			
M_B	Mass (M_J)	–	$97.5^{+4.4}_{-4.2}$
R_B	Radius (R_J)	[0,3]	$1.66^{+0.78}_{-0.55}$
P	Period (days)	–	$27.215250^{+0.000150}_{-0.000140}$
T_C	Time of conjunction (BJD$_{\rm TDB}$)	–	$2458576.18670^{+0.00160}_{-0.00160}$
a	Semi-major axis (AU)	–	$0.1819^{+0.0041}_{-0.0039}$
i	Inclination (Degrees)	–	$88.85^{+0.12}_{-0.12}$
e	Eccentricity	–	$0.4983^{+0.0025}_{-0.0022}$
ω_*	Argument of Periastron (Degrees)	–	$-63.2^{+0.2}_{-0.2}$
T_{eq}	Equilibrium temperature (K)	–	628^{+21}_{-21}
K	RV semi-amplitude (m s^{-1})	–	$7199.0^{+23.0}_{-22.0}$
δ	Transit depth (fraction)	–	$0.02900^{+0.03200}_{-0.01500}$
τ	Ingress/egress transit duration (days)	–	$0.08320^{+0.00170}_{-0.00150}$
T_{14}	Total transit duration (days)	–	$0.16640^{+0.00330}_{-0.00300}$
b	Transit impact parameter	–	$1.067^{+0.088}_{-0.066}$
ρ_P	Density (cgs)	–	$26.0^{+62.0}_{-18.0}$
$\log g_{\rm P}$	Surface gravity	–	$4.940^{+0.350}_{-0.340}$
$\langle F \rangle$	Incident flux (10^9 erg s^{-1} cm^{-2})	–	$0.03^{+0.00}_{-0.00}$

Wavelength parameters		R	Sloani	TESS
u_1	linear limb-darkening coeff	$0.476^{+0.053}_{-0.053}$	$0.316^{+0.054}_{-0.052}$	$0.337^{+0.052}_{-0.054}$
u_2	quadratic limb-darkening coeff	$0.303^{+0.048}_{-0.049}$	$0.231^{+0.046}_{-0.049}$	$0.249^{+0.050}_{-0.051}$

RV parameters		CHIRON	CORALIE	FEROS
$\gamma_{\rm rel}$	Relative RV Offset (m s^{-1})	24533^{+16}_{-17}	25958^{+36}_{-39}	25976^{+33}_{-33}
σ_J	RV Jitter (m s^{-1})	34^{+28}_{-22}	51^{+31}_{-39}	52^{+30}_{-26}
σ_J^2	RV Jitter Variance	1200^{+2700}_{-1000}	2600^{+4200}_{-2500}	2700^{+4000}_{-2100}

Notes. Priors are for the EXOFASTv2 global model only, where $\mathcal{G}$[a,b] are Gaussian priors. The topmost parameters were not modeled with EXOFASTv2 and the source of their value is displayed.